

How well can cold-dark-matter substructures account for the observed radio flux-ratio anomalies?

Dandan Xu^{1*}, Dominique Sluse^{2, 3}, Liang Gao^{4, 5, 6}, Jie Wang^{4, 6}, Carlos Frenk⁵, Shude Mao^{4, 6, 7, 8}, Peter Schneider³, Volker Springel^{1, 9}

¹Heidelberg Institute for Theoretical Studies, Schloss-Wolfsbrunnengasse 35, 69118 Heidelberg, Germany

²Institut d’Astrophysique et de Géophysique, Université de Liège, Allée du 6 Août 17, B5c, 4000 Liège, Belgium

³Argelander-Institut für Astronomie, Universität Bonn, Auf dem Hügel 71, 53121 Bonn, Germany

⁴National Astronomical Observatories, Chinese Academy of Sciences, 100012 Beijing, China

⁵Institute for Computational Cosmology, Dept. of Physics, University of Durham, South Road, Durham DH1 3LE, United Kingdom

⁶Key Laboratory for Computational Astrophysics, National Astronomical Observatories, Chinese Academy of Sciences, 100012 Beijing, China

⁷Jodrell Bank Centre for Astrophysics, the University of Manchester, Alan Turing Building, Manchester M13 9PL, United Kingdom

⁸Physics department and Tsinghua Center for Astrophysics, Tsinghua University, 100084, Beijing, China

⁹Zentrum für Astronomie der Universität Heidelberg, ARI, Mönchhofstr. 12-14, 69120 Heidelberg, Germany

Accepted Received ; in original form.....

ABSTRACT

Discrepancies between the observed and model-predicted radio flux ratios are seen in a number of quadruply-lensed quasars. The most favoured interpretation of these anomalies is that CDM substructures present in lensing galaxies perturb the lens potentials and alter image magnifications and thus flux ratios. So far no consensus has emerged regarding whether or not the predicted CDM substructure abundance fully accounts for the lensing flux anomaly observations. Accurate modelling relies on a realistic lens sample in terms of both the lens environment and internal structures and substructures. In this paper we construct samples of generalised and specific lens potentials, to which we add (rescaled) subhalo populations from the galaxy-scale Aquarius and the cluster-scale Phoenix simulation suites. We further investigate the lensing effects from subhalos of masses several orders of magnitude below the simulation resolution limit. The resulting flux ratio distributions are compared to the currently best available sample of radio lenses. The observed anomalies in B0128+437, B0712+472 and B1555+375 are more likely to be caused by propagation effects or oversimplified/improper lens modelling, signs of which are already seen in the data. Among the quadruple systems that have closely located image triplets/pairs, the anomalous flux ratios of MG0414+0534 can be reproduced by adding CDM subhalos to its macroscopic lens potential, with a probability of 5% – 20%; for B0712+472, B1422+231, B1555+375 and B2045+265, these probabilities are only of a few percent. We hence find that CDM substructures are unlikely to be the whole reason for radio flux anomalies. We discuss other possible effects that might also be at work.

Key words: gravitational lensing: strong - galaxies: haloes - galaxies: structure - cosmology: theory - dark matter.

1 INTRODUCTION

Understanding the radio flux ratios of multiply-imaged quasars has been a long-standing problem. In these systems, standard parametric models of the lens mass distribution (e.g., a singular isothermal ellipsoid plus external shear, hereafter “SIE+ γ ”) can fit the image positions well, but not

their flux ratios. This is known as the “anomalous flux ratio” problem (Kochanek 1991).

A number of solutions have been proposed. For example, some of the flux-ratio anomalies could be accommodated by adding higher order multipoles to the ellipsoidal potential of the lensing galaxy. However, the required amplitudes are deemed to be unreasonably larger than typically observed in galaxies and halo models (Evans & Witt 2003; Kochanek & Dalal 2004; Congdon & Keeton 2005; Yoo et al. 2006).

* E-mail: Dandan.Xu@h-its.org

Propagation effects in the interstellar medium, such as galactic scintillation and scatter broadening, could also cause anomalous flux ratios. If so, one would expect a strong wavelength dependence of the anomalies measured at radio wavelengths, which was not seen (Koopmans et al. 2003; Kochanek & Dalal 2004). Moreover, neither of the two solutions proposed above could explain the observed parity dependence of the flux anomalies (e.g., Metcalf & Madau 2001; Schechter & Wambsganss 2002; Keeton 2003; Kochanek & Dalal 2004).

Currently the most favoured explanation of the radio flux-ratio anomalies invokes the perturbation effects from small-scale structures hosted by lensing galaxies. In the cold dark matter (CDM) model of structure formation a large population of dark matter subhalos is predicted to survive inside larger “host” halos. In galaxies like the Milky Way, their number vastly exceeds the number of observed satellites (about two dozen have been discovered in the Milky Way to date). On the one hand, part of this discrepancy can be readily understood on the basis of standard ideas, e.g., photo reionization and stellar feedback on galaxy formation (Bullock et al. 2000; Benson et al. 2002; Bovill & Ricotti 2009; Cooper et al. 2010; Font et al. 2011; Guo et al. 2011). The gap was also narrowed by the discovery of a population of ultrafaint satellites from the Sloan Digital Sky Survey (SDSS) (Tollerud et al. 2008; Koposov et al. 2008, 2009). Despite this, several controversies still exist on small scales regarding the abundance (“missing satellite” problem, e.g., Klypin et al. 1999; Moore et al. 1999; Kravtsov et al. 2004) and the density profiles (“the cusp/core” problem, see Ludlow et al. 2013) of these dark matter subhalos that are predicted to exist but somehow failed to make galaxies.

If they do exist as CDM predicted, they could then be probed through their gravitational lensing effects. Earlier studies from e.g., Mao & Schneider (1998), Metcalf & Madau (2001) and Metcalf & Zhao (2002), proposed that substructures (on scales much smaller than image separations of $1''$ for typical lens and source redshifts) could explain the radio flux-ratio anomalies in quadruply-lensed quasar images. Later studies showed that the presence of substructures in lensing galaxies can also explain the observed tendency for the brightness of the saddle image to be suppressed (Schechter & Wambsganss 2002; Keeton 2003; Kochanek & Dalal 2004). The perturbations by subhalos have therefore emerged as one of the most convincing explanations for the radio flux-ratio anomalies. If true, such an explanation could have important implications for cosmology since it provides a direct and crucial test of the CDM model.

To date, there are about a dozen studies that use N -body simulations to test if the predicted CDM substructures have the right amount to explain the observed frequency of anomalous lenses in currently available samples. However, no consensus has emerged. While some of the studies (e.g., Dalal & Kochanek 2002; Bradač et al. 2004; Dobler & Keeton 2006; Metcalf & Amara 2012) suggest consistency between the CDM model and observations, others (e.g., Mao et al. 2004; Amara et al. 2006; Macciò et al. 2006; Macciò & Miranda 2006; Chen et al. 2011) including those by us (Xu et al. 2009, 2010) find that subhalos from CDM simulations are actually *insufficient* to explain the observed radio flux-anomaly frequency.

To tackle this problem from the numerical simulation point of view, one needs to model a realistic sample of the lens population, from their larger-scale environment to their internal structures and substructures. Any numerical experiment in this regard is facing several major issues that directly affect the accuracy of the study. For example, as shown by Keeton et al. (2003), flux ratios are quite sensitive to the ellipticity of the main lens. Metcalf & Amara (2012) also pointed out that one of the reasons that our previous studies (Xu et al. 2009, 2010) did not reproduce enough perturbations to match observations could be due to our adoption of a restricted ellipticity instead of the full range of ellipticities in the main lens models.

Second, the lack of a proper subhalo population may have distorted our previous conclusion. Previously we exclusively used the Milky Way-sized halos from the Aquarius project (Springel et al. 2008). However, massive elliptical galaxies, which comprise 80%-90% of observed lenses (Keeton et al. 1998; Kochanek et al. 2000; Rusin et al. 2003) are more likely to occur in group-sized halos which are generally ten times more massive. Since the subhalo abundance increases rapidly with increasing host halo mass (e.g. De Lucia et al. 2004; Gao et al. 2004; Zentner et al. 2005; Wang et al. 2012), the adoption of subhalo populations hosted by Milky Way-sized halos could underestimate the probability of flux-ratio anomalies.

Third, at present, even the best cosmological N -body simulations only resolve subhalos down to $10^{6\sim 7} h^{-1} M_{\odot}$ so the lensing effects from subhalos of masses beyond such resolution limit cannot be readily studied using these N -body simulations. In the cold dark matter cosmogony, low mass subhalos are much more abundant than their higher mass counterparts. Should we expect more perturbation effects from the low mass subhalos? Or what could be the observational signatures of these substructures predicted to exist at the lower levels of the hierarchy of cosmic structures? Specifically, down to which mass levels would the dark matter subhalos still be able to affect the image brightness and flux ratios at radio wavelengths?

Last but not least, the cosmological simulations that have been used in these studies contain only dark matter but no baryons, the inclusion of which might change the subhalo survival rate as well as their density profiles/concentration, that in turn might lead to a different conclusion.

In this paper we accommodate the first three issues above and find that for systems with image triplets/pairs of larger separation, whose flux ratios are less susceptible to density fluctuations, their observed anomalies are more likely to be caused by propagation effects or simplified lens modelling; for systems with closely located triplets/pairs, CDM substructures alone can only account for the observed flux ratios with percent-level probabilities; therefore they may not be the entire reason. We point out that other possible sources, e.g., inadequate lens modelling again, as well as baryonic substructures may also be at work. To this end, high resolution hydrodynamic simulations are in great need to help us identifying other possible culprits for the radio flux-ratio anomalies.

This paper is organized as follows: in the first part, we show that using generalised lens models and simulated subhalo populations in group-sized halos will indeed increase the flux anomaly frequency. Specifically, in Sect. 2 we review

the generic relations in cusp (Sect. 2.1) and fold (Sect. 2.2) lenses, and present our observational sample of eight systems, all of which have radio measurements for both cusp and fold relations (Sect. 2.3). In Sect. 3, we present the method to model massive elliptical lenses and their subhalo populations. For the former (in Sect. 3.1), we use a technique similar to that of Keeton et al. (2003). For the latter (in Sect. 3.2), we rescale the subhalo populations from two sets of high-resolution cosmological CDM simulations - the Aquarius (Springel et al. 2008) and Phoenix (Gao et al. 2012), and add them to the smooth lens potentials.

In the second part of this paper, i.e., in Sect. 4, we focus on individual observed systems, taking the best-fitting macroscopic lens models and populate not only the rescaled Aquarius and Phoenix subhalo populations above $10^7 h^{-1} M_\odot$ (in Sect. 4.2) but also a low-mass subhalo population down to masses two orders of magnitudes below (in Sect. 4.3 and 4.4). The observational signatures of very low mass subhalos and the dependence on source sizes are also studied and results are presented in Sect. 4.5. The probabilities to reproduce the observed flux ratios are given in Sect. 4.6. Finally a discussion and our final conclusions are given in Sect. 5.

The cosmology we adopt here is the same as that for both sets of simulations that we use in this work, with a matter density $\Omega_m = 0.25$, cosmological constant $\Omega_\Lambda = 0.75$, Hubble constant $h = H_0/(100 \text{ km s}^{-1} \text{ Mpc}^{-1}) = 0.73$ and linear fluctuation amplitude $\sigma_8 = 0.9$. These values are consistent with cosmological constraints from the WMAP 1- and 5-year data analyses (Spergel et al. 2003; Komatsu et al. 2009), but differ from the Planck 2013 results (Planck Collaboration et al. 2014), where $h = 0.67$ and $\sigma_8 = 0.83$. We do not expect these differences in cosmological parameters to have significant consequences for our conclusions.

2 GENERIC RELATIONS IN CUSP LENSES AND FOLD LENSES

There are three generic configurations of four-image lenses (see Fig. 1): (1) a source located near a cusp of the tangential caustic will produce a “cusp” configuration, where three images form close to each other around the critical curve on one side of the lens; (2) a source located near the caustic and between two adjacent cusps will produce a “fold” configuration, where a pair of images form close to each other near the critical curve; (3) a source located far away from the caustic, i.e., in the central region of the caustic, will produce a “cross” configuration, where all four images form far away from each other and away from the critical curve. Close triple images in cusp lenses and close pair images in fold lenses are the brightest images among the four, as they form close to the (tangential) critical curve.

There are some universal magnification relations for the triple and pair images in cusp and fold systems in smooth lens potentials. Without detailed lens modelling for individual systems, these generic relations assist one in identifying small-scale perturbations, which cause violations of these generic magnification relations.

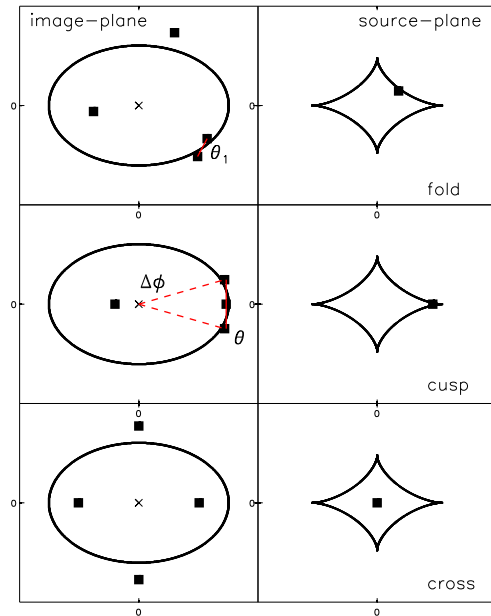


Figure 1. Three basic image configurations: fold (top), cusp (middle), and cross (bottom), with respect to the tangential critical curves in the image plane (on the left), and corresponding source positions with respect to the central caustics in the source plane (on the right). The image separation θ_1 of a close pair is labelled for the fold configuration; image opening angle $\Delta\phi$ and separation θ of a close triplet are labelled for the cusp configuration.

2.1 The cusp relation

In any smooth lens potential that produces multiple images (of a single source) of a cusp configuration, a specific magnification ratio (i.e., also flux ratio) of the image triplet will approach zero asymptotically, as the source approaches a cusp of the tangential caustic. This is known as the “cusp relation” (Blandford & Narayan 1986; Mao 1992; Schneider & Weiss 1992; Zakharov 1995; Keeton et al. 2003), mathematically defined as:

$$R_{\text{cusp}} \equiv \frac{\mu_A + \mu_B + \mu_C}{|\mu_A| + |\mu_B| + |\mu_C|} \rightarrow 0 \quad (\Delta\beta \rightarrow 0), \quad (1)$$

where $\Delta\beta$ is the offset between the source and the nearest cusp of the caustic, $\mu_{A,B,C}$ denote the triplet’s magnifications, whose signs indicate image parities.

Because $\Delta\beta$ cannot be directly measured, we therefore follow the practice of Keeton et al. (2003), using $\Delta\phi$ and $\theta/\theta_{\text{Ein}}$ to quantify a cusp image configuration. As labelled in Fig. 1, $\Delta\phi$ is defined as the angle between the outer two images of a triplet, measured from the position of the lens centre; $\theta/\theta_{\text{Ein}}$ is the maximum image separation among the triplet, normalized by the Einstein radius θ_{Ein} . In general, when the source moves towards the nearest cusp, both $\Delta\phi$ and $\theta/\theta_{\text{Ein}}$ will decrease to zero.

In particular small-scale structures, either within the lens or projected by chance along the line of sight, will perturb the lens potential and alter fluxes of one or more images. In this case, R_{cusp} will become unexpectedly large. The cusp relation, i.e., $R_{\text{cusp}} \rightarrow 0$ when $\Delta\beta \rightarrow 0$, will then be violated.

2.2 The fold relation

For an image pair in a fold configuration produced by any smooth lens potential, there is also a generic magnification relation, namely the “fold relation” (Blandford & Narayan 1986; Schneider & Weiss 1992; Schneider et al. 1992; Petters et al. 2001). In this paper, we take the form as in Keeton et al. (2005):

$$R_{\text{fold}} \equiv \frac{\mu_{\text{min}} + \mu_{\text{sad}}}{|\mu_{\text{min}}| + |\mu_{\text{sad}}|} \rightarrow 0 \quad (\Delta\beta \rightarrow 0), \quad (2)$$

where $\Delta\beta$ is the offset of the source from the fold caustic, $\mu_{\text{min,sad}}$ denote magnifications of the minimum ($\mu > 0$) and saddle ($\mu < 0$) images. To quantify a fold image configuration, similar to the practice of Keeton et al. (2005), we use $\theta_1/\theta_{\text{Ein}}$ to indicate how close the pair of images are. As labelled in Fig. 1, $\theta_1/\theta_{\text{Ein}}$ is defined as the separation, in unit of the Einstein radius θ_{Ein} , between the saddle image and the nearest minimum image.

Once again, when small-scale structures are present, R_{fold} will also become unexpectedly large; the fold relation, i.e., $R_{\text{fold}} \rightarrow 0$ when $\Delta\beta \rightarrow 0$, will then be violated. In principle one can study the perturbing small-scale structures by investigating the violations of the cusp and fold relations in extreme systems where $\Delta\beta \sim 0$. However, the detection of such systems is rare. For observed lenses, $\Delta\beta \neq 0$; and the exact values of R_{cusp} and R_{fold} depend on $\Delta\beta$, as well as the lens potentials. Without detailed lens modelling, one can identify cases of violations as outliers of some general distributions of R_{cusp} and R_{fold} for smooth lenses. A series of comprehensive and detailed studies on this topic have been carried out by e.g., Keeton et al. (2003, 2005), whose methods are largely followed in this work (Sect. 3.1).

2.3 A sample of cusp and fold lenses

In order to quantify how well the CDM substructures can account for the flux-anomaly observations, we take all the quadruple systems with R_{cusp} and R_{fold} measured at radio wavelengths, as the fluxes measured at optical and NIR (Sluse et al. 2013) wavelengths can be significantly affected by stellar microlensing and dust extinction. This forms a sample of a total of eight lenses; three “cusp”, and five “fold” lenses. The radio flux ratios of several other systems can also be found in literature but are excluded from this work: three systems have atypical nature of the lensing galaxy, i.e., the Einstein cross Q2237+0305 (Falco et al. 1996) which is lensed by the bulge of a spiral galaxy, the large separation system J1004+4112 (Jackson 2011) which is lensed by a galaxy cluster, and B1359+154 (Rusin et al. 2001) which shows six images and is lensed by a group of galaxies; we also excluded MG2016+112 (Garrett et al. 1994) which is only triply imaged at radio wavelengths.

To quantify the image geometry we take the basic image configuration measurements, namely, $\Delta\phi$, $\theta/\theta_{\text{Ein}}$ and $\theta_1/\theta_{\text{Ein}}$, as well as the measured and model-predicted flux ratios of R_{cusp} (for the closest triple images) and R_{fold} (for the closest saddle-minimum image pairs), as listed in Table 1. It can be seen that discrepancies at different levels exist between the measured flux ratios and model predictions. Below we give a brief description of each individual system in our lens sample.

2.3.1 B0128+437

This is a fold system. The observed flux ratios are likely affected by complex systematic errors, as suggested by radio-frequency dependent flux ratios and by VLBI imaging. The VLBI data show that the source is composed of three aligned components, one being tentatively associated with a flat spectrum core and the other two with steep spectrum components of the jet. The lensed image *B* only barely shows the “triple” structures, which are visible in images *A*, *C* and *D*. Hence it is likely that image *B* is affected by scatter broadening (Biggs et al. 2004). On the other hand, lens modelling using the VLBI data suggests astrometric perturbations of image positions by substructures (Biggs et al. 2004).

2.3.2 MG0414+0534

This is a fold system with a pair of images very close to the critical curve (image magnifications $|\mu| > 15$, see the lens modelling in Sect. 4). The low-resolution radio observations of Lawrence et al. (1995) lead to roughly the same R_{cusp} at multiple epochs and at different frequencies with the VLA, suggesting that the time delay between the lensed images is not a concern. However, a lower value of R_{cusp} was obtained from higher-resolution VLBI observations of Ros et al. (2000), which resolved the core+jet components of the source. The ratios for the core images also agree well with the one measured in MIR (Minezaki et al. 2009). The R_{fold} values from VLA, VLBI, MIR and extinction-corrected optical data all agree with each other within the measurement uncertainties. We use the VLBI results of both R_{cusp} and R_{fold} (for the core images) in our analysis.

2.3.3 B0712+472

This is a cusp/fold system with a close image configuration of $\Delta\phi = 76.9^\circ$. We use VLA flux ratios obtained at 5GHz by Koopmans et al. (2003). Those ratios were observed to be stable over 41 epochs of monitoring spanning 8.5 months, and are compatible with VLBI 5GHz measurements (Jackson et al. 2000). The flux ratios deviate significantly from the optical/NIR flux ratios, which are affected by differential extinction and microlensing (Jackson et al. 1998, 2000).

2.3.4 B1422+231

This is a classical cusp lens with $\Delta\phi = 77^\circ$. The flux ratios taken here were measured at different radio frequencies, at different epochs and with different spatial resolutions (with VLA and VLBA), which all agree with each other, as well as with mid-infrared (MIR) data (Patnaik et al. 1992, 1999; Koopmans et al. 2003; Chiba et al. 2005). Recently, with the aid of the adaptive optics integral field spectrograph on the Keck I Telescope, Nierenberg et al. (2014) derived the narrow-line flux ratios, which are also consistent with those measured in the radio.

2.3.5 B1555+375

This is a fold system, with a pair of images predicted to be very close to the critical curve (image magnifications $|\mu| > 50$). The radio fluxes were obtained at 5GHz with the VLA

and averaged over 41 epochs over 8.5 months (Koopmans et al. 2003). The HST images of this system also suggest that it is a very flattened lens.

2.3.6 B1608+656

This is a two-lens system, and has a fold image configuration with a relatively large opening angle. Lens models suggest that the image magnifications are small ($|\mu| < 5$). Many VLA data are available (including monitoring data) for this system and show consistently $R_{\text{fold}} \sim 0.32$. The radio measurements of R_{cusp} and R_{fold} are larger than observed in the optical and NIR, where the source appears to be extended and significantly affected by differential extinction (Surpi & Blandford 2003).

2.3.7 B1933+503

This is also a fold system and lens models suggest that the image magnifications are small ($|\mu| < 5$). The VLBI images presented in Suyu et al. (2012) reveal that the cores in images 1 and 4 show two peaks but not for image 3. This suggests that scatter broadening may modify the radio flux ratios. The R_{cusp} and R_{fold} obtained from this high resolution images also agree with lower resolution VLA and MERLIN data (Sykes et al. 1998), which are used here.

2.3.8 B2045+265

This is a very extreme cusp lens with $\Delta\phi = 34.9^\circ$. All three images are located (symmetrically) close to the critical curve with image magnifications $|\mu| > 50$. The radio flux ratios are very robust at different spatial resolution (VLA, VLBA) over different periods of time, and consistent with the H-K wavelengths (Fassnacht et al. 1999; McKean et al. 2007). Koopmans et al. (2003) identified significant intrinsic variability at radio wavelengths, but the amplitude of this effect is apparently small, at least on a time scale of months. The VLBA data reveals a core+jet emission for image *A*, but not for the saddle point image *B*, which should be brighter than *A* according to the models.

3 STATISTICAL FLUX-RATIO DISTRIBUTIONS

In this section, we study the statistical impact of CDM substructures on flux ratios. For this purpose, we generate mock galaxies of generic smooth lens potentials and with morphological properties similar to those of galaxies from SDSS. We then add to them subhalo populations from the Aquarius (Springel et al. 2008) and the Phoenix (Gao et al. 2012) simulations. This enables us to forecast R_{cusp} and R_{fold} distribution expected for a large sample of lensed systems and study the impact of the halo properties on these distributions. In Sect. 3.1 we present the method to model the generic lens potentials of massive elliptical lenses, and in Sect. 3.2 how we model their substructure populations. We describe the technique used to mock a statistical sample of quadruply-lensed quasars in Sect. 3.3. Finally results are given in Sect. 3.4.

3.1 Smooth lens model

To model the main lens halo (which is responsible for producing quadruply-lensed images), we adopt the approach from Keeton et al. (2003), with which we predict generic distributions for the cusp and fold relations.

Keeton et al. (2003, 2005) have shown that the flux (ratio) distributions have a weak dependence on the radial profile (from point mass to isothermal) of the lens mass distribution, but are sensitive to ellipticity e ($\equiv 1 - q$, where q is the axis ratio), higher-order multipole amplitude a_m and external shear γ_{ext} . In this work, we use a generalised isothermal ellipsoidal profile with an Einstein radius of $1.0''$ and also take into account the three aspects above. The detailed lens modelling and definitions for the parameters are described in the Appendix.

For choosing e and a_m , we use the result from Hao et al. (2006), who measured ellipticities and higher-order multipoles ($m = 3, 4$) of galaxies from SDSS. The mean and scatter of these shape parameters (mean $\bar{e} = 0.23$, dispersion $\sigma_e = 0.13$, mean $\bar{a}_3 = 0.005$, dispersion $\sigma_{a_3} = 0.004$, mean $\bar{a}_4 = 0.010$, dispersion $\sigma_{a_4} = 0.012$) are comparable to the values reported for the galaxy samples used in Keeton et al. (2003, 2005).

We note that by using the observed galaxy morphology distributions, we implicitly assume that the shape of dark matter (and thus total) density profiles follows baryons in the inner parts of the halo where strong lensing occurs. This has been supported by lensing observations from e.g., Koopmans et al. (2006) and Sluse et al. (2012).

It is also worth noting that although we draw shape parameters (e and a_m) from a galaxy sample at lower redshifts ($z < 0.2$), as addressed in Keeton et al. (2003, 2005), these distributions are not expected to be significantly different from those of the observed lensing galaxies at intermediate redshifts; observations have shown no significant evolution in the mass assembly history of early-type galaxies since $z \approx 1$ (Thomas et al. 2005; Koopmans et al. 2006).

Finally, the lens environment (e.g., Keeton et al. 1997) is accounted for by applying an external shear γ_{ext} drawn from a lognormal distribution with a median of 0.05 and a dispersion of 0.2 dex, same as in Keeton et al. (2003).

When adding simulated CDM subhalos to the generalised host lens potentials, we take 3600 different projections of subhalo distributions (see Sect. 3.2), and add each projected distribution to one of the host lens potentials. In order to maintain the possible correlation between ellipticities and high-order multipoles, we draw the combination of measured (e, a_3, a_4) from the observed galaxy sample of Hao et al. (2006). For each realization, we also take a randomly orientated external shear to add to the generalised isothermal ellipsoid.

3.2 CDM subhalos from the Aquarius and Phoenix simulations

To populate smooth lens potentials with CDM substructures, we take two sets of high-resolution cosmological N -body simulations: the Aquarius (Springel et al. 2008) and Phoenix (Gao et al. 2012) simulation suites. The former is composed of six Milky Way-sized halos ($M_{200} \sim 10^{12} h^{-1} M_\odot$) and the latter consists of nine galaxy cluster-

Table 1. Observed lenses with measurements of R_{cusp} and R_{fold} for the close triple images:

Lens	Type	$\Delta\phi(^{\circ})$	$\theta/\theta_{\text{Ein}}$	R_{cusp}	$\theta_1/\theta_{\text{Ein}}$	R_{fold}	References
B0128+437 [†]	fold	123.3	1.511	-0.043 ± 0.020 (-0.090)	0.584	0.263 ± 0.014 (0.161)	1, 2
MG0414+0534	fold	101.5	1.841	0.213 ± 0.049 (0.118)	0.388	0.087 ± 0.065 (-0.029)	3, 4, 5, 6
B0712+472	cusp	76.9	1.503	0.254 ± 0.024 (0.083)	0.243	0.085 ± 0.030 (-0.037)	1, 7, 8, 9
B1422+231	cusp	77.0	1.643	0.187 ± 0.004 (0.110)	0.636	-0.030 ± 0.004 (-0.131)	1, 10, 11, 3
B1555+375	fold	102.6	1.735	0.417 ± 0.026 (0.199)	0.365	0.235 ± 0.028 (0.023)	1, 12
B1608+656 ^{††}	fold	99.0	1.997	0.492 ± 0.002 (0.568)	0.831	0.327 ± 0.003 (0.411)	13, 14
B1933+503 [†]	fold	143.0	1.605	0.389 ± 0.017 (0.040)	0.884	0.656 ± 0.009 (0.257)	15, 16, 17
B2045+265	cusp	34.9	0.762	0.501 ± 0.020 (0.030)	0.253	0.267 ± 0.027 (-0.163)	1, 9, 18, 19

Notes: the quoted R_{cusp} and R_{fold} values in Col. 5 and 7 are measured at the radio wavelengths; their uncertainties are derived from the uncertainties in flux measurements (see Table A1 for the measured fluxes of the close triple images). Values in the parentheses are predicted by our best-fitting lens model, see Sect. 5.1. (†) Flux ratios are likely affected by systematic errors due to scattering. (††) Quoted fluxes are after correction for the time delays. References: (1) Koopmans et al. 2003; (2) Phillips et al. 2000; (3) Falco et al. 1999; (4) Lawrence et al. 1995; (5) Katz et al. 1997; (6) Ros et al. 2000; (7) Jackson et al. 1998; (8) Jackson et al. 2000; (9) Cfa-Arizona Space Telescope Lens Survey (CASTLES, see <http://cfa-www.harvard.edu/castles>); (10) Impey et al. 1996; (11) Patnaik et al. 1999; (12) Marlow et al. 1999; (13) Koopmans & Fassnacht 1999; (14) Fassnacht et al. 1996; (15) Cohn et al. 2001; (16) Sykes et al. 1998; (17) Biggs et al. 2000; (18) Fassnacht et al. 1999; (19) McKean et al. 2007; .

sized halos ($M_{200} \sim 10^{15} h^{-1} M_{\odot}$; M_{200} here is referred to as the virial mass, defined as the mass within R_{200} , the radius within which the mean mass density of the halo is 200 times the critical density of the Universe).

Observed lenses typically have an inner velocity dispersion of 200 – 300 km/s (e.g., Koopmans & Treu 2002; van de Ven et al. 2003), and some of them are also shown to live in the group environment (e.g., Momcheva et al. 2006; Wong et al. 2011). In comparison, the Aquarius halos have an equivalent inner velocity dispersion (estimated by $1/\sqrt{2}$ of the peak velocity) of ~ 150 km/s, and ~ 900 km/s for the Phoenix halos. We rescale all fifteen halos from both simulation suites to host halos of masses fixed at $M_{200} = 10^{12} h^{-1} M_{\odot}$, $10^{13} h^{-1} M_{\odot}$, and $5 \times 10^{13} h^{-1} M_{\odot}$. By doing so, we can study the lensing effects from subhalo populations hosted by halos on different mass scales and their dependences on host halo properties.

To be precise, we take both simulations at their second resolution levels, at which the minimum resolved subhalos have masses about seven orders of magnitude below the virial masses of their hosts. We define a rescaling factor \mathfrak{R} , which is the ratio between M_{200} of the arbitrary halo and that of a simulated halo. We rescale the masses of subhalos accordingly by a factor of \mathfrak{R} , and their velocities, sizes and halo-centric distances by a factor of $\mathfrak{R}^{\frac{1}{3}}$, so that the characteristic densities remain the same. It is noteworthy to mention that we only use M_{200} of individual halos to work out their rescaling factor. It is the subhalos (not the main halos) that we rescale and add to the constructed host lens potentials (as described in Sect. 3.1).

In the following, we present the rescaled subhalo properties, including mass function, characteristic velocities, sizes and spatial distributions.

3.2.1 Subhalo mass function

From Sect. 4.1 and Fig. 13 of Gao et al. (2012), no significant difference is seen between the shapes of subhalo mass functions of cluster-sized Phoenix halos and of Milky Way-sized Aquarius halos. The number of Phoenix subhalos is higher by 35% than the number of Aquarius subhalos at any fixed

subhalo-to-halo mass ratio m_{sub}/M_{200} . This is because clusters are dynamically younger than galaxies, therefore there are more subhalos surviving the tidal destruction.

3.2.2 Spatial distributions and projection effects

From Sect. 4.2 and Fig. 15 of Gao et al. (2012), the spatial distribution of the Phoenix subhalos is slightly more concentrated (more abundant near the centre) than that of the Aquarius subhalos due to the assembly bias effect, as the Phoenix simulations start from high density regions.

For this work, the projected spatial distribution of subhalos, especially in terms of the radial distribution of their surface number density, is of particular interest, as it directly influences the total lensing cross-section from subhalos. In this subsection, we show the mean projected spatial distributions obtained from averaging over hundreds of projections per host halo from both simulation suites.

Fig. 2 shows the projected subhalo number densities as a function of (projected) halo-centric distance up to $0.2R_{200}$. An important feature of the distribution is that it varies little with the projected halo-centric distances. Note that this is true (only) at smaller radii from the host centre and is also a result of the projection effect. More massive subhalos, e.g., $m_{\text{sub}} \gtrsim 10^9 h^{-1} M_{\odot}$, can only survive in the outer region of their host halo because of tidal destruction; their presence within the projected central $\sim 0.1R_{200}$ is purely due to chance alignment. We refer the reader to Springel et al. (2008, Fig. 11 and discussion therein) for the 3D spatial distribution of the subhalo population.

Also can be seen from Fig. 2 is that as the subhalo mass decreases by one decade, there is an increase by roughly a factor of ten in the number density of (projected) subhalos, i.e., $dN/d\ln m_{\text{sub}} \propto m_{\text{sub}}^{-1}$. This is in fact expected from the subhalo mass function ($dN/dm_{\text{sub}} \propto m^{-1.9}$, Springel et al. 2008), where the logarithmic slope is close to -2.0 . In Fig. 2, the Aquarius and Phoenix subhalos are rescaled to a host mass of $10^{12} h^{-1} M_{\odot}$; but the same features are also seen when they are rescaled to a host mass of $\gtrsim 10^{13} h^{-1} M_{\odot}$.

As the projected subhalo number densities remain constant in the inner part of a host halo, we take the mean

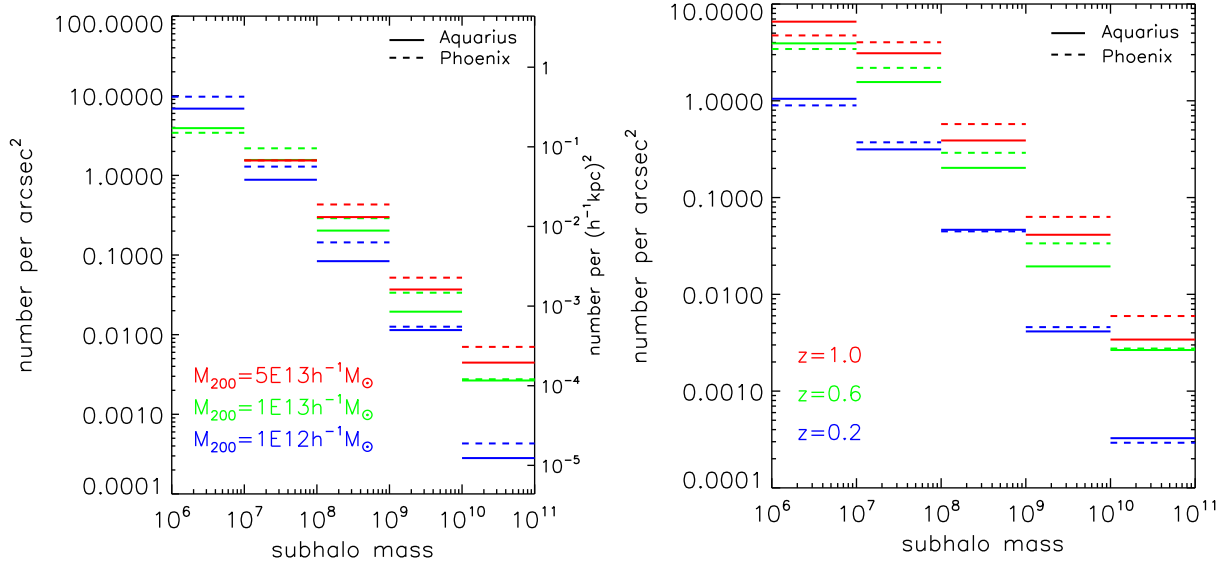


Figure 3. Projected subhalo number densities averaged within the central $R \leq 5''$ region, as a function of subhalo masses. The panel on the left shows the host mass dependence: subhalos taken at $z = 0.6$, their hosts rescaled to $M_{200} = 10^{12} h^{-1} M_{\odot}$ (blue), $10^{13} h^{-1} M_{\odot}$ (green) and $5 \times 10^{13} h^{-1} M_{\odot}$ (red). The right-hand side panel shows the redshift dependence: host halos are rescaled to $M_{200} = 10^{13} h^{-1} M_{\odot}$, taken at $z = 0.2$ (blue), $z = 0.6$ (green) and $z = 1.0$ (red). For both panels, 500 random projections are used per halo. The axis on the left-hand side of each panel gives number per sq. arcsec. The axis on the right-hand side of the left panel also gives number per sq. $h^{-1} \text{kpc}$ (in physical scale corresponding to a redshift at $z = 0.6$). Solid lines show the number densities of the Aquarius subhalos; dashed lines are for the Phoenix subhalos.

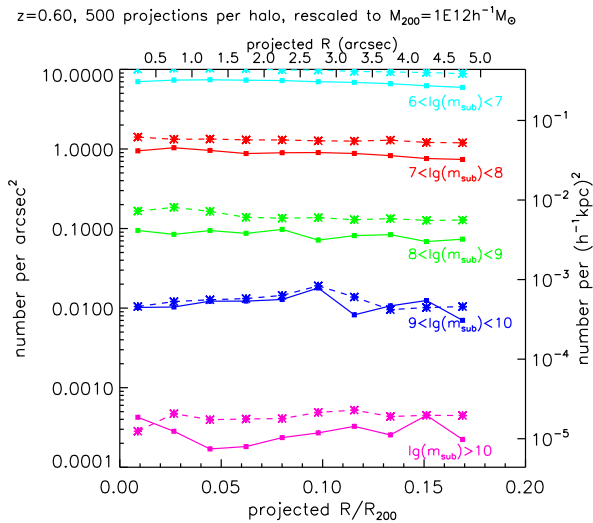


Figure 2. The radial distributions of projected subhalo number densities, averaged over six Aquarius halos (solid lines) and nine Phoenix halos (dashed lines) at redshift $z = 0.6$; 500 random projections are used per halo. All subhalo populations are rescaled to $10^{12} h^{-1} M_{\odot}$. Five different subhalo-mass ranges have been inspected: $10^{6 \sim 7} h^{-1} M_{\odot}$ (cyan), $10^{7 \sim 8} h^{-1} M_{\odot}$ (red), $10^{8 \sim 9} h^{-1} M_{\odot}$ (green), $10^{9 \sim 10} h^{-1} M_{\odot}$ (blue) and $> 10^{10} h^{-1} M_{\odot}$ (pink). The axis at the top gives the projected radius in arcsec; the one at the bottom gives the projected radius normalized to R_{200} . The axis on the left gives number per sq. arcsec; the one on the right gives number per sq. $h^{-1} \text{kpc}$ (in physical scale).

values averaged within the central $R \leq 5''$ region and studied their dependences on host halo mass and redshifts. Fig. 3 shows such mean number densities as a function of subhalo mass, plotted for host halos at three different M_{200} and three different redshifts. It can be seen that rescaling to more massive host halos will result in a higher number density of projected subhalos; the number per sq. arcsec also increases significantly with redshift.

Note that in Fig. 3 the lowest-mass bins below $10^7 h^{-1} M_{\odot}$ are only complete for host halos of $M_{200} = 10^{12} h^{-1} M_{\odot}$. Due to the simulation resolution limit, a level-two halo rescaled to $M_{200} = 10^{12} h^{-1} M_{\odot}$, $10^{13} h^{-1} M_{\odot}$ and $5 \times 10^{13} h^{-1} M_{\odot}$ would only host a complete subhalo sample down to a mass of $\sim 2 \times 10^5 h^{-1} M_{\odot}$, $\sim 2 \times 10^6 h^{-1} M_{\odot}$ and $\sim 10^7 h^{-1} M_{\odot}$, respectively. Above these “completeness” mass scales, one can easily read off the projected number densities η_{sub} for group-sized host halos ($M_{200} \gtrsim 10^{13} h^{-1} M_{\odot}$), which satisfy:

$$\frac{d\eta_{\text{sub}}}{d \ln m_{\text{sub}}} \approx 0.01 \left(\frac{m_{\text{sub}}}{3 \times 10^8 h^{-1} M_{\odot}} \right)^{-1} (h^{-1} \text{kpc})^{-2}. \quad (3)$$

The surface mass density in each mass decade is then estimated to be $\approx 3 \times 10^6 h^{-1} M_{\odot} (h^{-1} \text{kpc})^{-2}$. Consider a typical lens system with lens and source redshifts $z_1 = 0.6$ and $z_s = 2.0$, the critical surface mass density is $\Sigma_{\text{cr}} \approx 3 \times 10^9 h^{-1} M_{\odot} (h^{-1} \text{kpc})^{-2}$; then the surface mass fraction in substructures over five mass decades above $10^6 h^{-1} M_{\odot}$ amounts to $\lesssim 1\%$ around the critical curve, where the local convergence is $\kappa_{\text{cr}} \equiv \Sigma/\Sigma_{\text{cr}} \approx 0.5$. We mention in passing that the different subhalo mass fraction between here and 0.3% as in Xu et al. (2009) is attributed to a richer subhalo populations of group-sized halos considered here. These

fractions are also consistent with Vegetti et al. (2014), who searched for imprints of substructures in arc images of 11 gravitational lens systems from the Sloan Lens ACS Survey.

3.2.3 Subhalo density profiles

The peak circular velocity V_{\max} and the radius r_{\max} , at which V_{\max} is reached, are two important shape parameters for a subhalo's density profile. As can be seen from Fig. 14 of Gao et al. (2012), the relation between V_{\max} and r_{\max} is the same for the Aquarius and the Phoenix subhalos.

Springel et al. (2008) studied the density profile of subhalos and found them to be well fitted by Einasto profiles (Einasto 1965) with slope parameter $\alpha = 0.18$,

$$\rho(r) = \rho_{-2} \exp\left(-\frac{2}{\alpha} \left[\left(\frac{r}{r_{-2}}\right)^\alpha - 1\right]\right), \quad (4)$$

where ρ_{-2} and r_{-2} are the density and radius at which the local slope is -2 . For $\alpha = 0.18$, ρ_{-2} and r_{-2} are related to V_{\max} and r_{\max} by $r_{\max} = 2.189 r_{-2}$ and $V_{\max}^2 = 11.19 G r_{-2}^2 \rho_{-2}$, where G is the gravitational constant (see e.g., Springel et al. 2008 for more details about fitting Einasto profiles).

From both simulation sets, instead of taking particle distributions of subhalos for ray tracing, we take the measured V_{\max} and r_{\max} for each subhalo and assume an Einasto profile with $\alpha = 0.18$. We truncate the profile at a truncation radius r_{trnc} , which is set to be two times the half-mass radius r_{half} of the subhalo ($r_{\text{trnc}} = 2r_{\text{half}}$); the mass enclosed within such a truncation radius differs from the quoted subhalo mass m_{sub} by less than 10%. For subhalos below the resolution limit, we present the detailed method of deriving their profile parameters in Sect. 4.

We note that the Einasto parameter α could vary for different subhaloes (Vera-Ciro et al. 2013), and that r_{\max} cannot be measured as accurately as V_{\max} , especially for lower-mass subhalos. To see any potential change in the final result due to inaccurate measurements of subhalo profiles, we simply set r_{\max} of each subhalo to be 0.5, 1 and 2 times its current value and carry out the same lensing calculations.

Here we verify that there is no significant quantitative difference in the final flux ratio probability distributions resulting from different adoptions of r_{\max} . But we caution that when fundamentally different density profiles (in an extreme case a point mass) are chosen, the violation probabilities strongly depend on subhalo mass concentration (e.g., Rozo et al. 2006; Chen et al. 2011; Xu et al. 2012), which is not further discussed in this paper.

3.3 Generating a statistical sample of quadruply-lensed quasars

In this section, we predict the statistical distribution of the flux ratios (R_{cusp} and R_{fold}) of the quadruple images of background quasars. To this end, we mock a large sample of quadruply-lensed quasars assuming that they are point sources, which induce more violations to the cusp and fold relations than finite-sized sources.

For all the calculations presented in this section, we only take the (rescaled) Aquarius and Phoenix subhalos above $10^7 h^{-1} M_\odot$. For each subhalo that has a mass $m_{\text{sub}}^{78} \in [10^7 h^{-1} M_\odot, 10^8 h^{-1} M_\odot]$ and is projected in the central

strong lensing region, we artificially generate another ten subhalos each with a mass of $0.1 \times m_{\text{sub}}^{78}$, projected at the same halo-centric distance but with a random azimuthal angle. By doing so, we include a complete sample of subhalos at the $10^6 h^{-1} M_\odot$ scale.

There are two reasons for this choice of the lower mass limit. First, based on some simple finite source-size argument (e.g., Xu et al. 2012) such a mass scale was commonly used as subhalo lower mass limit in previous studies; the same adoption here will allow us to directly compare our results to those studies. Second, due to the nature of the subhalo mass function, the calculation done for low-mass subhalos will be significantly more expensive than that of their higher-mass counterparts. Therefore we neglect the contribution from subhalos below $10^6 h^{-1} M_\odot$ for the general statistical calculations here, but in Sect. 4, we carry out case studies using specific lens models to investigate the lensing effects from subhalos at several mass decades below $10^6 h^{-1} M_\odot$.

To eliminate biases due to halo-to-halo variations, we take a total of 3600 different projections of the simulated and rescaled subhalo distributions (over all redshifts) and add them to the generalised host lens potentials. To be precise, 300 projections were used for each of the six Aquarius halos and 200 projections for each of the nine Phoenix halos at different redshifts.

We assume the quasar redshift to be $z_s = 2.0$ and take simulated subhalo populations at five different lens redshifts: $z_l = [0.2, 0.4, 0.6, 0.8, 1.0]$, which follows the lens redshift span of the CLASS survey. We test two different redshift distributions: (1) a flat redshift distribution for the simulated subhalo populations, i.e., 60/40 projections per Aquarius/Phoenix halo at each of the five redshifts; and (2) a lensing cross-section weighted redshift distribution assuming the main lens to be a singular isothermal sphere with velocity dispersion $\sigma_{\text{SIS}} = 300$ km/s (and $z_s = 2.0$), which results in [26, 63, 79, 74, 58] projections per Aquarius halo and [17, 42, 53, 50, 38] projections per Phoenix halos at the five fixed redshifts, respectively. In terms of the final flux-ratio distributions, there is no significant difference between these two lens redshift distributions. In the subsections below we therefore present results obtained using the redshift distribution weighted by lensing cross-sections.

For each constructed lens potential, we carry out standard lensing calculations, similar to those used in our previous studies: a grid with resolution of $0.005''/\text{pixel}$ covers the lens plane, where deflection angles and second-order derivatives of the lens potentials from the host lens and from subhalos are calculated and tabulated on to the mesh. The adopted lens-plane resolution guarantees that the surface density distribution of the least massive subhalos at $m_{\text{sub}} \sim 10^6 h^{-1} M_\odot$ are resolved by a few to ten pixels at radii where their half masses and peak deflection angles are reached (see Fig. 6 in Sect. 4).

Source positions are uniformly distributed inside the tangential caustic (of each constructed lens) with a number density of 20000 per sq. arcsec, which naturally ensure that each realization is weighted by its four-image cross section in the source plane. The lensed images for any point source are found by solving the lens equation with a Newton-Raphson iteration method, setting the convergence error on image positions to be $0.0001''$. We do not consider magnification bias in our statistical analysis; possible consequences are dis-

cussed in a later section. In total we generate $\sim 5 \times 10^6$ four-image lens systems for final inspection of the cusp and fold violations.

3.4 Overall flux-ratio probability distributions

We calculate the flux-ratio probability distributions with a total of 5×10^6 realizations of generalised smooth lens potentials plus (rescaled) subhalo populations from the Aquarius and the Phoenix simulation suites.

The resulting flux-ratio probability distributions are presented in Fig. 4, where probability contours of $P(> |R_{\text{cusp}}|)$ for given $\Delta\phi$, $P(> |R_{\text{cusp}}|)$ for given $\theta/\theta_{\text{Ein}}$ and $P(> |R_{\text{fold}}|)$ for given $\theta_1/\theta_{\text{Ein}}$ are plotted. A small (large) probability P means that it is less (more) likely for a flux ratio, either $|R_{\text{cusp}}|$ or $|R_{\text{fold}}|$, to be larger than a given value, at a given image configuration, described by $\Delta\phi$, $\theta/\theta_{\text{Ein}}$ or $\theta_1/\theta_{\text{Ein}}$. The top panels show the result from adopting smooth models; the middle panels show results from using the smooth models plus a subhalo population hosted by a Milky Way-sized halo of $M_{200} = 10^{12} h^{-1} M_{\odot}$; the bottom panels present results from taking a subhalo population hosted by a group-sized halo of $5 \times 10^{13} h^{-1} M_{\odot}$. Note that these distributions do not vary with the way that data are binned when using a reasonable range of bin sizes.

To indicate the range of the observed flux ratios, on top of the probability contours in the top panel of Fig. 4, measured $|R_{\text{cusp}}|$ and $|R_{\text{fold}}|$ of the eight lenses in our sample are plotted as blue squares, together with measurement errors. Flux ratios that are predicted by the lens model that best fits the image astrometry are also given, plotted as cyan diamonds in the top panel.

It is important to realize that the forecasts shown in Fig. 4 do not take into account the magnification bias¹. Therefore the predictions cannot be directly compared to the measurements made for specific individual lenses; the calculations here are only aiming at finding an allowed range and distribution of R_{cusp} and R_{fold} .

The inclusion of substructures significantly broadens the flux ratio distributions and increases the probabilities at larger values (for close image configurations). As can be seen from the middle and bottom panels of Fig. 4, the values of R_{cusp} and R_{fold} measured for the observed lenses could indeed be reproduced by adding CDM substructures to the generalised host lens potential. The more massive the host halos are, the higher the probabilities for having large $|R_{\text{cusp}}|$ and $|R_{\text{fold}}|$. This is expected, as the number of subhalos increases with host halo mass (see Sect. 3.2).

Adding substructures significantly changes the flux-ratio probability distributions for the image triplets/pairs that have small separations, but does not strongly affect the distributions on larger scales. Such a variation behaviour confirms what one would expect from local density perturbations: the image magnification and local convergence satisfy

$\mu \approx (1 - 2\kappa)^{-1}$ and thus $\delta\mu/\mu \propto \mu\delta\kappa$ in the case of perturbation. A close image configuration means that the image pairs must be located close to the critical curves, where $\mu \rightarrow \infty$. Therefore a tiny density fluctuation $\delta\kappa$ around the image positions can cause a huge magnification fluctuation $\delta\mu$.

When a perturber is located near an image that is further away from the critical curves (i.e., in the case of larger pair separations), it is less efficient in altering the image magnification via a density fluctuation. However, it could, if massive enough, shift the image to a new position, where the magnification is different. In this case, standard lens models (neglecting relatively massive perturbers if they are not luminous enough to be seen) would have difficulties in fitting the image positions. This is also referred to as ‘‘astrometric anomaly’’ (e.g., Chen et al. 2007).

Due to the nature of the subhalo mass function, magnification variations due to image position shifting (caused by relatively massive subhalos) are expected to be less frequent than magnification perturbation resulting from local density fluctuations (of lower-mass subhalos), which will mainly occur for image pairs with small separations around the critical curves. This is consistent with the fact that only a small fraction of flux anomaly systems are also reported to have astrometric anomalies (Biggs et al. 2004; McKean et al. 2007; Sluse et al. 2012).

4 FLUX RATIO PROBABILITIES OF OBSERVED QUADRUPLE SYSTEMS

In Sect. 3, we demonstrated that the values of R_{cusp} and R_{fold} measured at radio wavelengths for the quadruply lensed systems could be reproduced by adding CDM substructures to generalised lensing galaxy potential/mass distribution. Unfortunately, this approach has its limitations in at least the following three aspects:

(1) Many lensing galaxies lie in rich environments (Momcheva et al. 2006; Wong et al. 2011). It is in general necessary to account for the nearest lensing galaxy or group explicitly in the model to reproduce the observed astrometry of those systems. Accounting for these companions can modify the flux ratios at the 30% level in some observed systems, but this can only be addressed on a case-by-case basis.

(2) A quantitative comparison between the forecast of Fig. 4 and the observational data requires a proper understanding of the selection effects of the sample, which should also be applied to the mocked data from simulations. Unfortunately, this is not the case here.

(3) In any survey, the magnification bias plays an important role in the selection of lens candidates, which enhances the probability to observe highly magnified systems. Quantifying this bias is however not an easy task. In addition, the flux ratios of those highly magnified systems are more susceptible to the vast amount of very low-mass subhalos, which were not included in the statistical calculations presented in Sect. 3.

For all these reasons, we use in this section an alternative methodology. We study the effects of CDM substructures in each individual lens in our sample (instead of a generic population of lenses) by adding substructures to a macro lens model that reproduces the observed astrometry,

¹ Without correction for magnification bias, highly-magnified systems cannot be fairly sampled. Indeed these events only occupy a small fraction of the central caustic region in the source plane and thus would have lower weight in the statistical sample. However, due to the huge magnification effect they would be among the brightest detections in the Universe.

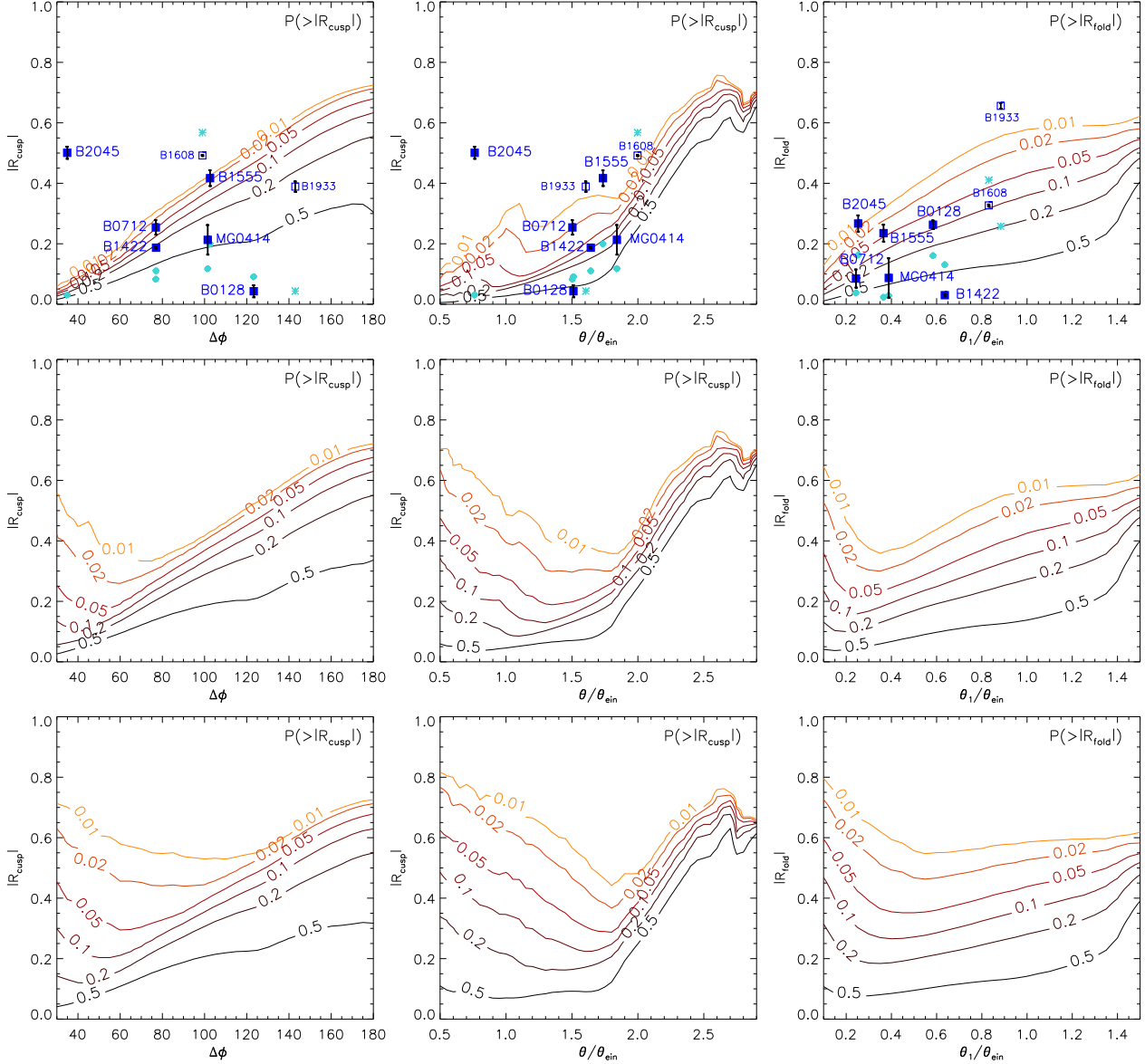


Figure 4. Probability contour maps of conditional probabilities $P(> |R_{\text{cusp}}|)$ for given $\Delta\phi$ (left column), $P(> |R_{\text{cusp}}|)$ for given $\theta/\theta_{\text{Ein}}$ (middle column) and $P(> |R_{\text{fold}}|)$ for given $\theta_1/\theta_{\text{Ein}}$ (right column). The meanings for $\Delta\phi$, $\theta/\theta_{\text{Ein}}$ and $\theta_1/\theta_{\text{Ein}}$ can be seen in Fig. 1. Contour levels of 1, 2, 5, 10, 20 and 50 per cent (from light to dark) are plotted. Top: singular isothermal ellipsoidal potentials with axis ratio q and higher-order perturbation amplitudes a_m drawn from 847 observed galaxies (Hao et al. 2006), plus randomly oriented external shear. Middle: smooth potentials (as above) plus perturbations from a simulated subhalo population hosted by a Milky Way-sized halo of $M_{200} = 10^{12} h^{-1} M_{\odot}$. Bottom: smooth potentials (as for the top panel) plus perturbations from a simulated subhalo population hosted by a group-sized halo of $M_{200} = 5 \times 10^{13} h^{-1} M_{\odot}$. More than 5×10^6 realizations have been calculated for each case. For indication, measured and model predicted flux ratios ($|R_{\text{cusp}}|$ and $|R_{\text{fold}}|$) of eight observed lenses are plotted as blue squares and cyan diamonds, respectively; measurement errors are also given.

and investigating the resulting flux ratio distributions of images that closely resemble the observed configurations.

We describe in Sect. 4.1 how we model the observed lenses, in Sect. 4.2 how we add (to the macroscopic lens models) the subhalo populations from the Aquarius and Phoenix simulation suites, and in Sect. 4.3 how we model the subhalos that have masses up to three orders of magnitude below the simulation resolution limit. The ray-tracing method is described in detail in Sect. 4.4. In Sect. 4.5, we carry out a case study using B2045+265 to investigate the observational

signatures of very low-mass subhalos and their dependence on source sizes. Finally, the flux ratio probability distribution for each of the observed systems are given in Sect. 4.6.

4.1 Macro models of the observed lenses

For the observed systems, we adopt a singular isothermal ellipsoid plus a constant external shear γ_{ext} to fit only astrometric measurements, i.e., positions of lensing galaxies, and (VLBI/VLA) positions of lensed images. We do not use

image flux ratios to constrain the best lens models. A second lens, being either a satellite galaxy or a galaxy group, is also included in the model if its optical/X-ray counterpart is seen in the same field (the induced shear then may not be treated as constant). This second lens is treated as a singular isothermal sphere (SIS).

Table 2 lists parameters of our standard lens models (SIE+ γ +SIS) for systems in our sample. The predicted R_{cusp} and R_{fold} of the close triple images (consistent with those from the literature) are given in the parentheses in Col. 5 and Col. 7 of Table 1.

We note that two systems, i.e., B1608+656 and B1933+503, have been excluded from such lens modelling and the discussions below, due to the following reasons:

(1) Both lenses are spiral/discy galaxies (Fassnacht et al. 1996; Sykes et al. 1998). This component has however little effect on the image positions and is mostly constrained by the flux ratios (Maller et al. 2000; Möller et al. 2003). We therefore do not expect that the simplified models adopted here are appropriate for these two lenses.

(2) The images in the close triplets (in both lenses) are located far away from the critical curve ($|\mu| < 5$). As explained in Sect. 3, local density perturbations are not expected to cause significant magnification variation. Therefore CDM substructures are unlikely to be responsible for the flux anomalies in these two cases.

4.2 Adding Aquarius and Phoenix subhalos to the macroscopic lens models

In order to maintain the macroscopic critical curve, we renormalize the macroscopic convergence κ_{mac} by a factor of $(1-\kappa_{\text{sub}})$, where κ_{sub} is the convergence from the total amount of subhalos (including the very low-mass ones) projected in the central region. We then add to the best-fitting macroscopic lens potentials the simulated subhalo populations at above $10^7 h^{-1} M_{\odot}$ taken from the snapshots with redshifts closest to the observed lens redshifts.

In this section, for each of the observed lenses, we rescale the simulated subhalo populations to match a host halo whose inner velocity dispersion (estimated by $1/\sqrt{2}$ of the peak velocity as first-order approximation) is equal to the one constrained by the best-fitting SIE model. The masses of the rescaled host halos that are supposed to host the observed lenses range from $10^{12} h^{-1} M_{\odot}$ (for B0128+437 and B1555+375) to $2.5 \times 10^{13} h^{-1} M_{\odot}$ (for B2045+265).

For each lens, we draw ~ 250 projections from each of the simulated host halos, i.e., ~ 3800 projections in total from all fifteen halos in the two simulation suites. For each realization (including adding very low-mass subhalos in Sect. 4.3), multiple candidate source positions within a radius of $0.01''$ around the model-constrained source position (with respect to the caustic) were searched for close triple images. Here we further adopt a selection criteria so that only systems that best resemble the observed image geometry would be chosen. The criteria are applied to the configuration parameters $\Delta\phi$, $\theta/\theta_{\text{Ein}}$ and θ_1/θ of the close triplets in each simulated system. We require the relative differences between the simulated and the observed quantities to be no

larger than 10%:

$$\begin{aligned} \left| \frac{(\Delta\phi)_{\text{sim}}}{(\Delta\phi)_{\text{obs}}} - 1 \right| &\leq 0.1, \\ \left| \frac{(\theta/\theta_{\text{Ein}})_{\text{sim}}}{(\theta/\theta_{\text{Ein}})_{\text{obs}}} - 1 \right| &\leq 0.1, \\ \left| \frac{(\theta_1/\theta)_{\text{sim}}}{(\theta_1/\theta)_{\text{obs}}} - 1 \right| &\leq 0.1. \end{aligned} \quad (5)$$

4.3 Model subhalos beyond the CDM simulation resolution limit

As an important complement to current studies, we investigate the lensing effects from subhalos with masses between $10^4 h^{-1} M_{\odot}$ and $10^7 h^{-1} M_{\odot}$. For simplicity and clarity, three specific masses fixed at $m_{\text{sub}} = 3 \times 10^4 h^{-1} M_{\odot}$, $3 \times 10^5 h^{-1} M_{\odot}$ and $3 \times 10^6 h^{-1} M_{\odot}$ are used for the three different mass decades in question. Assuming that the subhalo mass function and their profile parameters follow power-law functions of mass, we extrapolate the spatial distribution $\eta(R)$ and density profiles $\rho(r)$ of subhalos from the Aquarius and the Phoenix simulations to these very low-mass scales considered here. Three different source radii r_s of 1pc, 3pc and 5pc, reflecting the different sizes of the emission regions of lensed quasars, are also applied to investigate the source size dependence.

4.3.1 Projected number density distribution

The halo-centric distribution of the projected number densities $\eta_m(R)$ of the low-mass subhalos, where $m = 4, 5, 6$ for the three different mass bins studied here, are extrapolated from that of their higher-mass counterparts – the resolved subhalos from the rescaled Aquarius and Phoenix simulations. From Fig. 2, it can be seen that the subhalo number density $\eta(R)$ at a given mass decade almost remains constant in the inner region of their host. This density increases by a factor of 10 each time when subhalo masses decrease by one decade. We therefore model the projected number densities η_m of low-mass subhalos by: $\eta_m = \eta_{78} \times 10^{(7-m)}$, where at η_{78} is the projected number density of subhalos of $10^{7\sim 8} h^{-1} M_{\odot}$. The projected positions of the low-mass subhalos are then randomly distributed in the lens plane, according to their projected number densities η_m .

4.3.2 Density profiles

As in Sect. 3, we assume subhalos to be modelled by Einasto profiles (Einasto 1965) with slope parameter $\alpha = 0.18$. The other two parameters that are required to fix the profile are V_{max} and r_{max} , both of which are measured for the resolved subhalos in the Aquarius and Phoenix simulations (see Sect. 3.2.3). The sets of parameters V_{max} and r_{max} for the low-mass subhalos studied here are obtained by extrapolating the $V_{\text{max}} - m_{\text{sub}}$ and $r_{\text{max}} - V_{\text{max}}$ relations that exist, albeit not tight, for their higher-mass counterparts. Fig. 5 shows an example of the extrapolation using subhalos from one of the level-two Aquarius halos. As the fitting formula for the $V_{\text{max}} - m_{\text{sub}}$ and $r_{\text{max}} - V_{\text{max}}$ relations change little at

Table 2. Best SIE+ γ ($N_{\text{lens}} = 1$) and SIE+SIS+ γ ($N_{\text{lens}} = 2$) models for our sample:

Lens	z_1	z_s	N_{lens}	$\theta_{\text{Ein}}('')$	$e, \theta_e(\text{deg})$	$\gamma, \theta_\gamma(\text{deg})$	$\Delta G('')$	χ^2 (d.o.f.)	$\chi_{\text{ima}}^2, \chi_{\text{lens}}^2$
B0128+437 ¹	0.6	3.12	1	0.235	0.46, -27.72	0.213, 41.17	0.006	0.4 (1)	0.0, 0.4
MG0414+0534 ¹	0.96	2.64	2	1.100, 0.181	0.22, 82.65	0.099, -55.03	0.000	0.0 (0)	0.0, 0.0
B0712+472 ^{†2}	0.41	1.34	1	0.699	0.36, -61.8	0.076, -13.35	0.028	2.0 (1)	1.95, 0.06
B1422+231 [♣]	0.34	3.62	2	0.785, 4.450	0.21, -57.62	0.091, 77.47	0.000	0.0 (1)	0.0, 0.0
B1555+375 ^{♠3,4}	0.6	1.59	1	0.238	0.32, 81.26	0.143, -81.97	0.012	0.16 (1)	0, 0.16
B2045+265 ¹	0.87	1.28	2	1.101, 0.032	0.11, 29.09	0.203, -67.07	0.000	0.0 (0)	0.0, 0.0

Notes: Col. 4 gives the total number of lenses included for modelling; Col. 6 provides the best-fitting amplitude and orientation of the ellipticity; Col. 7 gives the external shear amplitude and the position angle of the shear mass; Col. 8 provides the observed lensing galaxy position with respect to the best-fitting lens position; Col. 9 provides the total χ^2 of the best-fitting lens model; Col. 10 provides the independent contribution from the image and lens astrometry to the total χ^2 . Note that flux ratios are not used to constrain the models. (†) Unrealistic lens models are obtained when the nearby group positions of Fassnacht & Lubin (2002) or Fassnacht et al. (2008) are used; therefore the group is not included in our lens modelling. (♣) This model uses the X-ray centroid of the group by Grant et al. (2004). (♠) We assume $(z_1, z_s) = (0.6, 1.59)$ and use the galaxy position from CASTLES, $(\Delta_{\text{galRA}}, \Delta_{\text{galDEC}}) = (-0.185, -0.150) \pm 0.03''$ with respect to image A. References: (1) Sluse et al. 2012; (2) Jackson et al. 2000; (3) Marlow et al. 1999; (4) CfA-Arizona Space Telescope Lens Survey (CASTLES, see <http://cfa-www.harvard.edu/castles>). Cohn et al. 2001.

redshift $z < 1$, we take the following uniform fitting expressions:

$$\begin{aligned} v_{\text{max}} &= 3.6 \text{ km s}^{-1} \left(\frac{m_{\text{sub}}}{10^6 h^{-1} M_\odot} \right)^{0.32} \\ r_{\text{max}} &= 0.55 \text{ kpc/h} \left(\frac{v_{\text{max}}}{10 \text{ km s}^{-1}} \right)^{1.34} \end{aligned} \quad (6)$$

Each subhalo will be truncated at a radius r_t , within which the enclosed mass is equal to the given subhalo mass, i.e., $m(\leq r_t) = m_{\text{sub}}$. At an assumed lens redshift $z_1 = 0.6$, subhalos of $m_{\text{sub}} = 3 \times 10^4 h^{-1} M_\odot$, $3 \times 10^5 h^{-1} M_\odot$ and $3 \times 10^6 h^{-1} M_\odot$ are truncated at $r_t = 0.03''$, $0.06''$ and $0.12''$, respectively. Fig. 6 shows the enclosed mass profile, convergence profile and the distribution of deflection angle as a function of projected radius.

With the Einasto-profile parameters fixed, lensing properties can be calculated at any given position in the lens plane. Once again we vary r_{max} by a factor of 0.71 and 0.58 from the default value (so that the overdensity $\delta \equiv (v_{\text{max}}/r_{\text{max}})^2$ varies by a factor of 2 and 3) and repeated the same calculation. We verify that such variations do not bring marked difference in the flux-ratio distributions.

4.4 Ray-tracing for the magnification calculation

The lensing effect of the low-mass subhalos strongly depends on the size of the emission region of the source, i.e., the smaller the latter is, the stronger the former would be. Our numerical approach needs to reproduce image magnifications for various source sizes.

To ensure that the regions of interests will be sampled with enough resolution, we use a finer lens-plane mesh with a resolution of $0.0002''/\text{pixel}$ that covers the observed image triplets to calculate the lensing properties (i.e., the first- and second-order derivatives of the lens potentials) of the main lens and of the subhalos. Again image positions and magnifications of a point source are found through a Newton-Raphson iteration method. To find the image magnifications of a finite-sized source at $\vec{\beta}^*$ with radius r_s , we start casting rays from the grid points $\vec{\theta}$ of the regular lens-plane mesh to the source plane according to the lens equation, all the resulting source positions $\vec{\beta}$ that satisfy $|\vec{\beta} - \vec{\beta}^*| \leq r_s$

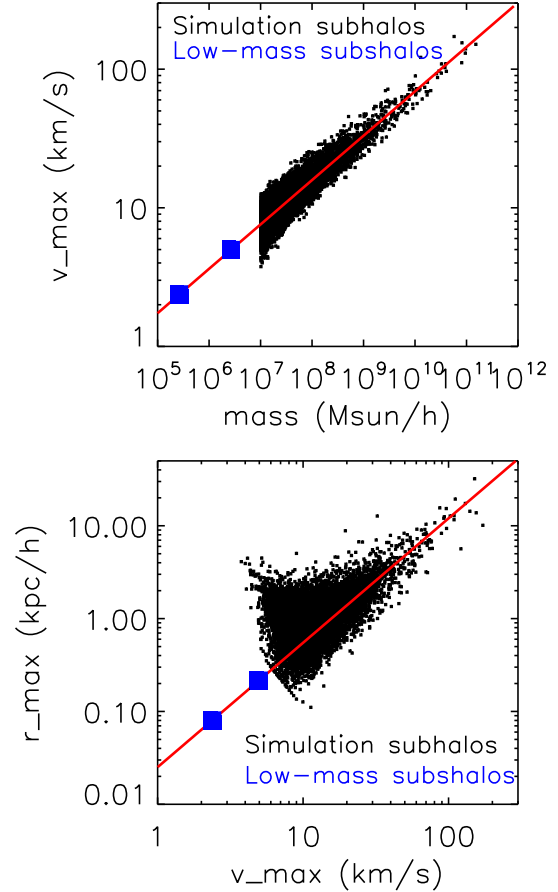


Figure 5. The extrapolation of the $V_{\text{max}} - m_{\text{sub}}$ and $r_{\text{max}} - V_{\text{max}}$ relations using subhalos (black dots) from one of the level-two Aquarius halos. The red lines are given by Eq. (6). The blue symbols represent the adopted values according to the relation for subhalos at $3 \times 10^5 h^{-1} M_\odot$ and $3 \times 10^6 h^{-1} M_\odot$.

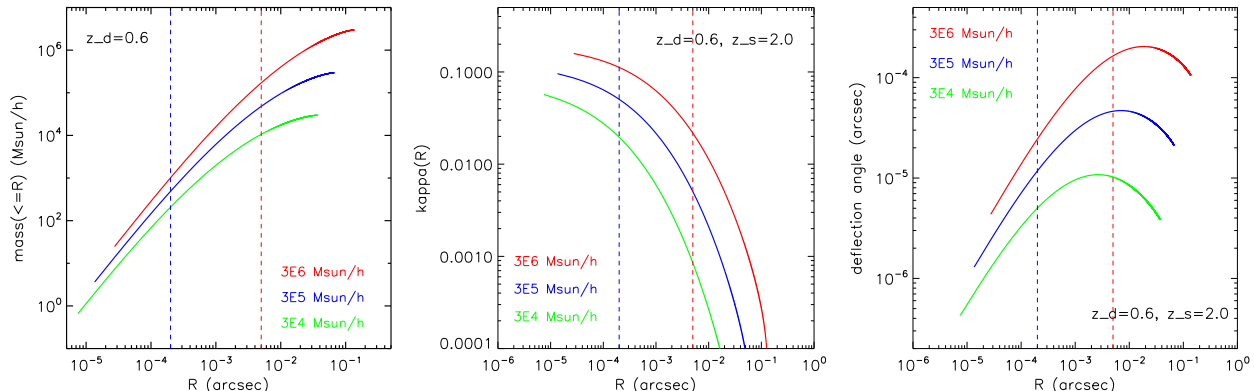


Figure 6. The enclosed mass (left), convergence (middle) and deflection angle (right) distributions as a function of radius for Einasto-profiled subhalos at $3 \times 10^4 h^{-1} M_\odot$ (green), $3 \times 10^5 h^{-1} M_\odot$ (blue) and $3 \times 10^6 h^{-1} M_\odot$ (red). The dashed red (blue) vertical line indicates the lens-plane mesh resolution used in the calculations presented in Sect. 3 (Sect. 4), which ensures that the least massive subhalos in question can be resolved by a few to ten pixels at radii where their half masses and peak deflection angles are reached.

are picked out. Their lens-plane counterparts map out three groups that correspond to the triple images of the given finite-sized source. The image magnification μ^* of each image is then given by:

$$\mu^* = \frac{\sum_i \delta\theta^2}{\sum_i \delta\beta_i^2} = \frac{\sum_i \delta\theta^2}{\pi r_s^2}, \quad (7)$$

where $\delta\theta^2$ is the uniformly-sampled finite area element in the image plane, and $\delta\beta^2 = \delta\theta^2/\mu_i$ is the corresponding area element in the source plane. The summation \sum_i is over all the test positions $\vec{\theta}_i$ that are mapped to the source plane where $|\vec{\beta}_i - \vec{\beta}^*| \leq r_s$.

4.5 Impact of very low-mass subhalos and the finite source effect

In this subsection, we investigate whether subhalos below the resolution limit, i.e., $\sim 10^7 h^{-1} M_\odot$, can still produce significant flux ratio anomalies. For this purpose we perform the case study of B2045+265: we take the macroscopic lens model and image geometry and calculate the perturbation effects from inclusion of subhalos of $m_{\text{sub}} = 3 \times 10^4 h^{-1} M_\odot$, $3 \times 10^5 h^{-1} M_\odot$ and $3 \times 10^6 h^{-1} M_\odot$. In particular, we study several cases with different combinations of subhalo properties and source sizes. In each case, we repeat the magnification calculation 2000 times to obtain different realizations of subhalo spatial distributions. The statistical distributions of image magnification ratios are case-dependent, and thus unveil how the perturbation effects from the very low-mass subhalos depend on their masses and source sizes.

As $\delta\mu/\mu \propto \mu\delta\kappa$, at around the main critical curve, even a small mass fluctuation $\delta\kappa$ (from subhalos) could modify the shape of the critical curve. This is demonstrated in Fig. 7, where an example using B2045+265 is given. In the case of very low-mass subhalos, localized critical lines could form around these perturbers on milli-arcsecond (mas) to sub-mas scales. When an image that is located near the main critical curve happens to cover these localized critical lines, the brightness of the image can be significantly enhanced if the image size is on similar scales ($\lesssim 0.001''$).

Fig. 8 shows the differential and cumulative probability

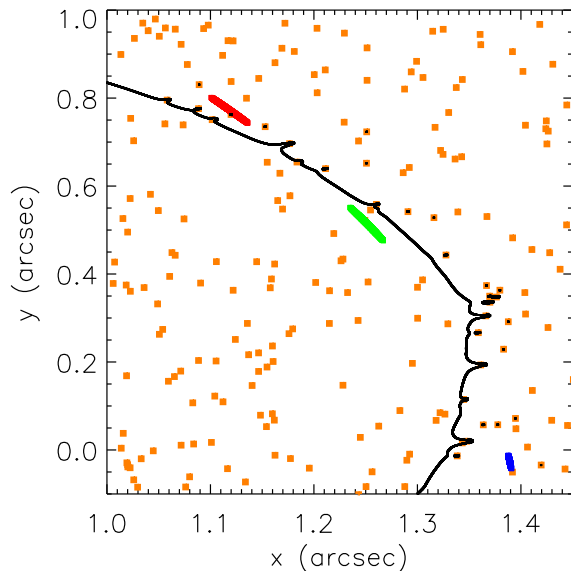


Figure 7. Tangential critical curve of B2045+265, small-scale wiggles and isolated local critical curves are induced by subhalos of $10^5 \sim 10^6 h^{-1} M_\odot$ (orange). Red, green and blue regions are the close triplets of the theoretical source with a finite radius of 5pc.

distributions of R_{cusp} and R_{fold} , calculated under different scenarios. The top panel presents results for a finite-sized source of a fixed radius but using three different subhalo masses. The bottom panel shows results for subhalos at a fixed subhalo mass but assuming a point source and a finite-sized source of different radii.

It is clearly seen that the perturbation effects on the flux ratios become significant with increasing subhalo masses m_{sub} , even though the number densities η_{sub} decrease. Convergence tests with different lens-plane resolution at $0.0001''$, $0.0002''$ and $0.0005''$ per pixel confirmed that such numerical results are genuine and not due to insufficient resolution. This is expected, as explained in Xu et al. (2009), because for simulated subhalos or point masses, the lensing cross-section σ of a subhalo can be approximated by

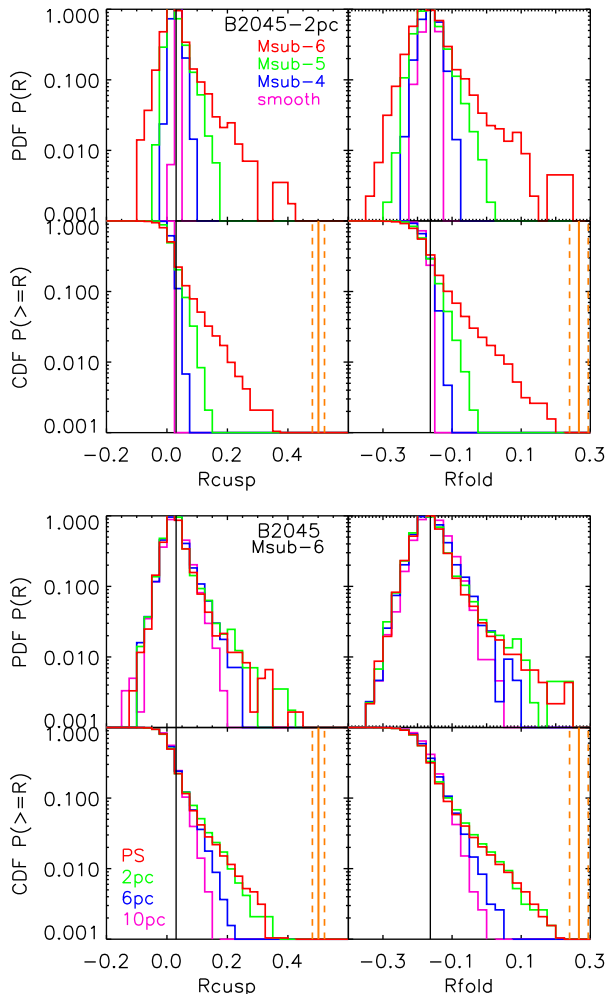


Figure 8. The differential and cumulative probability distributions of R_{cusp} (left) and R_{fold} (right), calculated under different scenarios. The top panel presents results for a finite-sized source of 1pc in radius, the included subhalo masses are at $3 \times 10^4 h^{-1} M_{\odot}$ (green), $3 \times 10^5 h^{-1} M_{\odot}$ (blue) and $3 \times 10^6 h^{-1} M_{\odot}$ (red) as well as in the absence of substructures (pink). The bottom panel shows results for subhalos at $3 \times 10^6 h^{-1} M_{\odot}$ but assuming a point source (red), a finite-sized source of 1pc (blue), 3pc (green) and 5pc (pink) in radii. Orange vertical lines indicate the measured flux ratios (and the uncertainties) for B2045+265.

$\sigma \propto m_{\text{sub}}^{\alpha}$, where α is a positive index, thus rendering the total lensing cross-section dominated by massive subhalos. For this reason, when calculating the flux-ratio probability distributions for each of the observed lenses, we safely neglect subhalos below $10^5 h^{-1} M_{\odot}$ so that the computational expense stays low.

On the other hand, when the subhalo mass is fixed, we see that the smaller the source size is, the more extended the distribution tail becomes; point sources yield the most significant extension at large flux ratios. In the next subsection, we therefore only present results for each observed system under the point source assumption to achieve an upper bound of possible substructure perturbation.

Another very interesting feature seen from Fig. 8 is that the distribution is skewed towards larger R_{cusp} (and R_{fold}). Such an asymmetric distribution is rooted in the

tendency that saddle (minimal) images become fainter (brighter) where clumpy substructures are present near the image positions. Such a behaviour from low-mass subhalos is similar to that shown in the bottom panel of Fig. 3 in Schechter & Wambsganss (2002).

4.6 Results for individual lenses

Below we present the flux-ratio probability distributions for each of the observed lens systems, calculated using their observed specific image configurations and their own lens models, plus CDM substructures above $10^5 h^{-1} M_{\odot}$. Fig. 9 shows the probabilities to have R_{cusp} and R_{fold} larger than the observed values in each systems.

As can be seen, such probabilities are about 5% – 20% (taking into account the large measurement uncertainties) for MG0414+0534. For the rest of the lenses in our sample, the probabilities are only 1% – 4%. In principle, the close image geometries of these systems should make their flux ratios more susceptible to density perturbations (e.g., from CDM substructures). However, such percent-level probabilities indicate that there must be other sources for the mismatch between the measured and model predictions. For example, VLBI observations already showed evidence of scatter broadening in B0128+437 (Biggs et al. 2004). For B0712+472, a galaxy group has been identified on its line of sight (Fassnacht & Lubin 2002, Fassnacht et al. 2008). We were unsuccessful in accounting for this group in the smooth lens model (Table 2) due to its uncertain X-ray centroid. The lens model for B1555+375 might also not be optimal, as the position angles of the ellipticity and of the external shear are nearly orthogonal; the HST images also suggest a flattened morphology. All these strongly indicate a possibly missing ingredient in the lens model. In the next section, we discuss other possible reasons to account for the discrepancy.

5 DISCUSSION AND CONCLUSIONS

5.1 The contribution from CDM substructures

In Sect. 3 we see (from the bottom panel of Fig. 4) that the inclusion of CDM substructures reproduces those large values of R_{cusp} and R_{fold} seen in observations. Indeed, among the observed lenses in our sample, McKean et al. (2007) found that a lens model that incorporates an observed dwarf satellite (the luminous counterpart of a dark matter subhalo) could reproduce all image positions as well as the flux ratios for B2045+265. MacLeod et al. (2013) also showed that the observed flux ratios in MG0414+0534 can be reproduced by adding a substructure of $\sim 10^7 M_{\odot}$ close to image A2. Again with detailed lens modelling, Nierenberg et al. (2014) found a better fit to the image astrometry as well as the flux ratios when adopting a lens model that includes a perturbing mass of $10^{7\sim 8} M_{\odot}$ around image A. Other works, e.g., Bradač et al. (2002), Dobler & Keeton (2006) and Fadely & Keeton (2012), also found that the inclusion of a local perturbation with mass of $10^{5\sim 8} M_{\odot}$ can always help to explain the image flux ratios measured at longer wavelengths.

On the one hand, the flux ratios can always be “fixed” by adding local density perturbations to the smooth lens

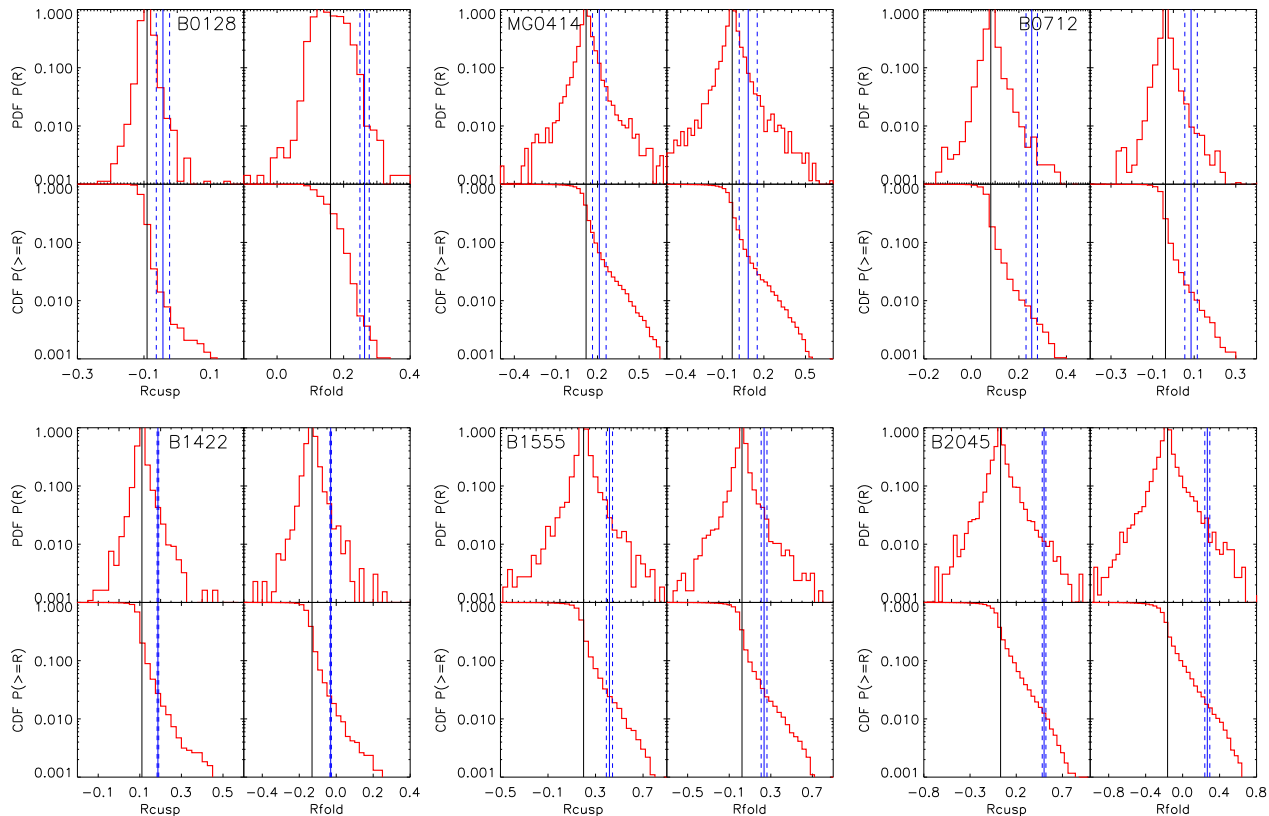


Figure 9. Flux ratio probability distributions (same as Fig. 8) for selected realizations that most resemble each observed system. Red solid lines represent results from including CDM substructures above $10^5 h^{-1} M_\odot$. Measured and predicted flux ratios are indicated by the blue and black vertical lines, respectively. Dashed lines indicate errors on the measurements.

potential that reproduce the observed macroscopic image positions. However, it is interesting that coincidentally the required masses of the added perturbers happen to be within a range that is predicted for abundant low-mass CDM subhalos that survive the tidal destruction during galaxy formation.

But on the other hand, when deploying a theoretical population of the CDM subhalos from cosmological simulations, we find that even for systems (like B1555+375 and B2045+265) that are more susceptible to local density perturbations, the probabilities to reproduce values of R_{cusp} and R_{fold} larger than the measured values are only at per cent level. This strongly indicates that there are other culprits for the radio flux-ratio anomalies. In the next subsection, we present these other possibilities.

We mention in passing that CDM substructures could not only affect the radio flux ratios of a multiply-imaged quasar, but also leave imprints on the surface brightness distribution of a lensed galaxy. Through the detection and modelling of these image distortions, one can also constrain the level of density perturbations in a mass range of $10^{6\sim 9} h^{-1} M_\odot$ in a lensing galaxy (Vegetti & Koopmans 2009). This has already been put into good practice by e.g., Vegetti et al. (2012, 2014) on the SLACS lenses using high resolution HST and Keck adaptive optics imaging. The resulting CDM substructure fraction is in consistent with the ones derived from N -body simulations (see Sect. 3.2.2). More high-resolution images of lensed dusty star-forming

galaxies will also soon be available from ALMA, which can also be used to constrain CDM substructures via the induced image distortion (Hezaveh et al. 2013).

5.2 Other culprits for radio flux-ratio anomalies

Xu et al. (2012) investigated the effects from CDM halos along the line-of-sight to a lensed quasar. Comparing Fig. 9 therein with Fig. 4 here, it can be seen that the contribution of these interlopers can be as important as that of the intrinsic CDM substructures within the lensing galaxy (also, e.g., Metcalf 2005a,b; Miranda & Macciò 2007). However even factoring in the effects from line-of-sight perturbers, the gap between the observed flux ratios and model predictions still remains.

In Xu et al. (2010), three types of substructures other than bound CDM subhalos were investigated, i.e., satellite galaxies, globular clusters (GC) and satellite streams, which were found to contribute little to solving the radio flux-ratio anomaly problem. However the adoption of an empirical Milky-Way GC population has a caveat. As also pointed out in their discussion, massive elliptical galaxies are known to host more GCs than their spiral counterparts (Forte et al. 1982; Harris 1991, 1993; West 1993). GCs are typically of mass $10^{5\sim 6} M_\odot$ and have the most compact density profiles among all known types of galactic substructures. We would hence like to point out the possibility of massive

elliptical GC populations to be an extra source of relevant perturbations for our problem.

Apart from GCs, baryonic substructures may also exist at above the $10^6 M_\odot$ level. When a small halo merges with a bigger halo, and later on becomes a subhalo, sinking towards the inner region of the host, its dark matter component could be significantly stripped due to tidal destruction, leaving behind a baryon-dominated overdensity. This is because the latter is much more concentrated than the former and thus less prone to tidal stripping. Such baryonic substructures ($10^{7\sim 9} M_\odot$) may follow a similar or an even more concentrated spatial distribution compared to their CDM subhalo counterparts; their density profiles (being more compact) differ completely from the latter due to the different nature of baryons and dark matter. These surviving baryonic substructures of a similar mass range as their CDM counterparts may also induce significant density perturbations and thus cause radio flux anomalies. Interestingly Shin & Evans (2008) investigated the possibility of using the Milky-Way satellite galaxy population to explain the observed flux anomaly frequencies. They found that the results strongly depend on the applied density profiles (of the baryonic substructures); a central density enhancement relative to the Milky-Way satellite population of a factor of 10 – 100 is needed in order to explain observations.

Other possible sources of radio flux anomalies also include oversimplified/improper lens modelling and radio propagation effects, for which there is already evidence in a few systems (e.g., B0128+437, B0712+472, B1555+375), and might have affected the model-predicted flux ratios therein.

5.3 Summary

Discrepancies between the observed and model-predicted flux ratios that assume a smooth lens are seen in a number of radio lenses. The most favoured interpretation of these anomalies is that CDM substructures perturb the lens potentials and alter image magnifications (and thus flux ratios). In this work we particularly study the cusp and fold relations in quadruple lenses to see how the flux ratios R_{cusp} and R_{fold} would be affected by CDM substructures.

In the first part of this paper, we assume that general smooth lens potentials can be modelled as isothermal ellipsoids with a wide range of axis ratios, higher-order multipole perturbations and randomly oriented external shear (Sect. 3.1). We then take two sets of state-of-the-art high resolution CDM cosmological simulations: the Aquarius suite of galactic halos and the Phoenix suite of cluster halos whose subhalo populations were rescaled to those expected in group-sized halos (Sect. 3.2). By ray-tracing through the combined (and perturbed) lens potentials, we produce a large sample of quadruply-imaged quasars lensed by massive elliptical galaxies, and predict their flux ratio probability distributions.

We find that host mass rescaling indeed makes a difference in the final R_{cusp} and R_{fold} probability distributions (see Fig. 4). The projected radial distribution of the surface number density of subhalos, as well as their dependence on host halo masses and redshifts, are given in Fig. 2 and 3. The subhalo mass fraction at around one Einstein radius increases by a factor of 3 from Milky Way-sized host ha-

los to group-sized host halos (Sect. 3.2.2). As a result, using subhalo populations in group-sized halos markedly increases the flux anomaly frequencies compared to using those from Milky Way-sized halos (Sect. 3.4). The forecasts as shown in Fig. 4 also clearly confirm that systems which are more likely to show signatures of CDM substructures through the induced anomalous flux ratios are those with small image opening angle and/or image separation, or in other words, highly magnified systems.

In the second part of this paper, we present results of case studies for observed lens systems, all of which have radio measurements for both cusp and fold relations. In these calculations we take the best-fitting macroscopic lens models (Sect. 4.1), populating the rescaled Aquarius and Phoenix subhalo populations above $10^7 h^{-1} M_\odot$ (due to resolution limit, see Sect. 4.2), and subhalos with masses three orders of magnitudes lower (Sect. 4.3). Through numerical experiments we confirm that perturbation effects increase with increasing subhalo mass (assuming point sources); but decrease with increasing size of a finite source (Fig. 8). We then study the probability distributions of R_{cusp} and R_{fold} for mock samples that closely resemble the specific image geometries in the observed systems, predicting how likely it is to reproduce the measurements for each system in presence of CDM subhalos (Sect. 4.6).

Focusing on those systems with closely located image triplets/pairs, as can be seen from Fig. 9, we find that to have R_{cusp} and R_{fold} larger than the observed values the probabilities are only 1% – 4% for most systems. Only for MG0414+114, a probability of 5% – 20% is obtained. We conclude that CDM substructures may not be the entire reason for the radio flux anomaly problem; other sources, e.g., propagation effects and/or inadequate lens modelling, could also be at work. Apart from those, baryonic (sub)structures with masses ranging from $10^6 M_\odot$ to $10^9 M_\odot$ that survive the tidal destruction during galaxy merger and accretion could also be important sources of density fluctuation and thus (radio) flux ratio anomalies.

Comparisons between the results from two different methodologies performed in this paper as well as in existing literature on flux ratio anomalies (see Sect. 1) suggest that a proper study of flux ratio anomalies needs a well-controlled sample of lenses. Alternatively, investigations based on individual systems may critically depend on the choice of the reference macroscopic model to which substructures are added. More specifically, the nearby lens environment can modify R_{cusp} (and R_{fold}) at a level of tenths of percents; variation in ellipticity and deviations from perfect ellipses in the lens mass distribution (parametrized with multipole terms) can also lead to significant changes of the flux ratios. Therefore, apart from local density perturbations, simplified lens modelling which does not take into account the ingredients above can also lead to a spurious mismatch between the observed and the predicted flux ratios.

To make further progress on this problem, on the one hand more detailed observations, e.g., higher resolution and deeper image and spectroscopic data of the quadruple systems are needed to allow better characterization and quantification of macro lens models; on the other hand, high resolution hydrodynamic simulations that follow the evolution of baryons as well as the interplay between baryons and dark

matter are necessary to assist in identifying all true culprits for the radio flux-ratio anomalies.

ACKNOWLEDGEMENTS

The authors would like to thank Matthias Bartelmann, Olaf Wucknitz, Ben Metcalf, Simona Vegetti, Neal Jackson, Leon Koopmans and Caina Hao for insightful discussion, and thank Aaron Ludlow for providing test data and useful comments. This work was carried out partly on the DiRAC-1 and DiRAC-2 supercomputing facilities at Durham University, and partly on the Magny supercomputing facilities at HITS. DDX acknowledges the Alexander von Humboldt foundation for the fellowship. DS is supported by the German *Deutsche Forschungsgemeinschaft*, DFG project No. SL172/1-1, and by a *Back to Belgium* grant from the Belgian Federal Science Policy (BELSPO). This project is supported by the Strategic Priority Research Programme “The Emergence of Cosmological Structures” of the Chinese Academy of Sciences Grant No. XDB09000000 (LG, JW, and SM). LG acknowledges supports from the 100-talents program of the Chinese academy of science (CAS), the National Basic Research Program of China - Program 973 under grant No. 2009CB24901, the NSFC grants No. 11133003, the MPG Partner Group Family and the STFC Advanced Fellowship, and thanks the hospitality of the Institute for Computational Cosmology (ICC) at Durham University. JW acknowledges supports from the Newton Alumni Fellowship, the 1000-young talents program, the 973 program grant No. 2013CB837900, 2015CB857005, the CAS grant No. KJZD-EW-T01, and the NSFC grant No. 11373029, 11390372, 11261140641. CSF acknowledges an ERC Advanced Investigator grant (COSMIWAY). SM thanks the CAS and National Astronomical Observatories of CAS (NAOC) for financial support. VS acknowledges financial support from the Deutsche Forschungsgemeinschaft through Transregio 33, ‘The Dark Universe’. Phoenix is a project of the Virgo Consortium. Most simulations were carried out on the Lenova Deepcomp7000 supercomputer of the super Computing Center of CAS in Beijing. This work was also supported in part by an STFC Rolling Grant to the ICC.

Table A1. Observed lenses with measurements of R_{cusp} and R_{fold} for the close triple images:

ID	Observation	F_1	F_2	F_3	R_{cusp}	R_{fold}	Images	References
B0128 [†]	VLA 5 GHz 41 epochs	0.584 ± 0.029	1.0 ± 0.0	0.506 ± 0.032	-0.043 ± 0.020	0.263 ± 0.014	B*-A-D*	1
	VLBA 5 GHz	2.8 ± 0.28	10.6 ± 1.06	4.8 ± 0.48	-0.165 ± 0.055	0.582 ± 0.034	-	2
	Merlin 5 GHz	9.5 ± 1	18.9 ± 1	9.2 ± 1	-0.005 ± 0.046	0.331 ± 0.033	-	3
MG0414	VLBI 8.5 GHz core	115.6 ± 11.56	97 ± 9.7	34 ± 3.4	0.213 ± 0.049	0.087 ± 0.065	A1-A2*-B	4
	VLA 15 GHz 4 epochs	157.0 ± 5.5	138.75 ± 5	138.75 ± 2.25	0.361 ± 0.012	0.062 ± 0.024	-	5
	MIR	1.0 ± 0.0	0.9 ± 0.04	0.36 ± 0.02	0.204 ± 0.016	0.053 ± 0.020	-	6
B0712	VLA 5 GHz 41 epoch	1.0 ± 0.0	0.843 ± 0.061	0.418 ± 0.037	0.254 ± 0.024	0.085 ± 0.030	A-B*-C	1
	VLBA 5 GHz	10.7 ± 0.15	8.8 ± 0.15	3.6 ± 0.15	0.238 ± 0.009	0.097 ± 0.010	-	7
B1422	VLA 5 GHz 41 epochs	1.0 ± 0.0	1.062 ± 0.009	0.551 ± 0.007	0.187 ± 0.004	-0.030 ± 0.004	A-B*-C	1
	VLBA 8.4 GHz	152 ± 2	164 ± 2	81 ± 1	0.174 ± 0.006	-0.038 ± 0.009	-	8
B1555	VLA 5 GHz 41 epochs	1.0 ± 0.0	0.62 ± 0.059	0.507 ± 0.073	0.417 ± 0.026	0.235 ± 0.028	A-B*-C	1
B1608 ^{††}	VLA 8.5 GHz	2.045 ± 0.01	1.037 ± 0.01	1.0 ± 0.001	0.492 ± 0.002	0.327 ± 0.003	A-C*-B	9
B1933 [†]	VLBA 5 GHz	4.7 ± 0.4	19.4 ± 0.4	5.4 ± 0.4	0.315 ± 0.016	0.610 ± 0.009	3*-4-6*	10
	VLA 15 GHz	2.5 ± 0.4	15.5 ± 0.4	3.2 ± 0.4	0.462 ± 0.018	0.722 ± 0.009	-	10
B2045	VLA 5 GHz 41 epochs	1.0 ± 0.0	0.578 ± 0.059	0.739 ± 0.073	0.501 ± 0.020	0.267 ± 0.027	A-B*-C	1
	VLBA 5 GHz	1.0 ± 0.01	0.61 ± 0.01	0.93 ± 0.01	0.520 ± 0.003	0.242 ± 0.007	-	11

Notes: the fluxes and errors (in Col. 3, 4 and 5) are directly taken from the literature in their original units. When flux errors are not available, we take 10% of the measured fluxes as their uncertainties. Image names (in Col. 8) associated with * indicate the images with negative parities. (†) Flux ratios are likely affected by systematic errors due to scattering. (††) Quoted fluxes are after correction for the time delays. References (1) Koopmans et al. 2003; (2) Biggs et al. 2004 (Table 3); (3) Phillips et al. 2000; (4) Ros et al. 2000; (5) Lawrence et al. 1995; (6) Minezaki et al. 2009; (7) Jackson et al. 2000; (8) Patnaik et al. 1999; (9) Fassnacht et al. 1999; (10) Sykes et al. 1998; (11) McKean et al. 2007.

APPENDIX A: SUMMARY OF THE BEST FLUX RATIOS FOR THE SAMPLE OF LENSED SYSTEMS

We provide in Table A1 the best available flux ratio measurements for the sample of lenses studied in the main text. When flux ratios vary with spatial resolution due to resolved structures in images, we provide measurements obtained at different spatial resolution. When available, we also report flux ratios averaged over several epochs or corrected for time delays between images. In Table A1, VLBA and VLBI images have typical beam sizes of 2 sq. mas while VLA and MERLIN frames have typical beam sizes of 50 sq. mas.

APPENDIX B: GENERALISED ISOTHERMAL LENS WITH MULTIPOLE PERTURBATION AND EXTERNAL SHEAR

Consider a lens potential composed of a singular isothermal ellipsoidal, m^{th} -mode multipole perturbation and external shear:

$$\psi(\theta, \phi) = \psi_{\text{SIE}}(\theta, \phi) + \psi_m(\theta, \phi) + \psi_{\text{ext}}(\theta, \phi), \quad (\text{B1})$$

where θ and ϕ are the image position $\vec{\theta} = (\theta_x, \theta_y)$ in polar coordinate: $\theta = \sqrt{\theta_x^2 + \theta_y^2}$ and $\phi = \tan^{-1}(\theta_y/\theta_x)$; ψ_{SIE} , ψ_m and ψ_{ext} are lens potentials of an singular isothermal ellipsoidal, m^{th} -mode multipole perturbation and external shear, respectively. In our numerical approach for lensing calculations, we tabulate to a Cartesian mesh (θ_x, θ_y) in the image plane values of the reduced deflection angle and second-order derivatives of the lens potential.

For a generalised isothermal lens (plus perturbations), the lens potential ψ and convergence κ follow the pair of equations below (Keeton et al. 2003, Appendix B2):

$$\begin{aligned} \psi(\theta, \phi) &= \theta F(\phi) = \theta \left[F_{\text{SIE}}(\phi) + \sum_{m=3,4} F_m(\phi) \right], \\ \kappa(\theta, \phi) &= R(\phi)(2\theta)^{-1} = \left[R_{\text{SIE}}(\phi) + \sum_{m=3,4} \delta R_m(\phi) \right] (2\theta)^{-1}. \end{aligned} \quad (\text{B2})$$

From the Poisson equation $\nabla^2 \psi = 2\kappa$, $F(\phi)$ and $R(\phi)$ are related by: $R(\phi) = F(\phi) + F''(\phi)$. $F_{\text{SIE}}(\phi)$ and $R_{\text{SIE}}(\phi)$ are shape functions of a singular isothermal ellipsoidal lens, while $F_m(\phi)$ and $\delta R_m(\phi)$ describe the higher-order multipole perturbations. For the generic lens model used in this work, only $m = 3$ and 4 are considered.

B1 Singular isothermal ellipsoid

Specifically, if the isothermal ellipsoid's major and minor axes coincide with the Cartesian axes, then the shape functions are given by (Kassiola & Kovner 1993; Kormann et al. 1994; Keeton & Kochanek 1998):

$$\begin{aligned} R_{\text{SIE}}(\phi) &= \frac{\theta_{\text{Ein}}}{\sqrt{1 - \epsilon \cos 2\phi}}, \\ F_{\text{SIE}}(\phi) &= \frac{\theta_{\text{Ein}}}{\sqrt{2\epsilon}} \left[\cos \phi \tan^{-1} \left(\frac{\sqrt{2\epsilon} \cos \phi}{\sqrt{1 - \epsilon \cos 2\phi}} \right) + \sin \phi \tanh^{-1} \left(\frac{\sqrt{2\epsilon} \sin \phi}{\sqrt{1 - \epsilon \cos 2\phi}} \right) \right]. \end{aligned} \quad (\text{B3})$$

where θ_{Ein} is the Einstein radius of the singular isothermal ellipsoid, $\epsilon = (1 - q^2)/(1 + q^2)$ and $q \in (0, 1]$ is the axis ratio of the ellipsoid. It can be shown that $R_{\text{SIE}}(\phi)$ is the equation in polar coordinates of the ellipse at the critical curve, where $\kappa_{\text{SIE}} = \frac{1}{2}$. $R_{\text{SIE}}(\phi)$ corresponds to the ellipse's equation in Cartesian coordinates:

$$\frac{\theta_x^2}{a^2} + \frac{\theta_y^2}{b^2} = 1, \quad \text{where } a = \frac{\theta_{\text{Ein}}}{\sqrt{1 - \epsilon}}, \quad b = aq = \frac{\theta_{\text{Ein}}}{\sqrt{1 + \epsilon}}. \quad (\text{B4})$$

As convergence $\kappa_{\text{SIE}}(\theta, \phi) = \frac{R_{\text{SIE}}(\phi)}{2\theta}$, the iso- κ_{SIE} contours follow the ellipse $R_{\text{SIE}}(\phi)$ and are scaled by θ^{-1} .

B2 Higher-order multipole perturbations

Now consider adding a higher-order multipole perturbation $\delta R_m(\phi)$ to the iso- κ ellipse $R_{\text{SIE}}(\phi)$, where $\delta R_m(\phi)$ is defined as (see Keeton et al. 2003, Appendix B2):

$$\delta R_m(\phi) = a_m \cos(m(\phi - \phi_m)) \quad (\text{B5})$$

where $a_m (>0)$ and ϕ_m are the amplitude and ‘‘orientation’’ of the m^{th} -order perturbation to the perfect ellipse $R_{\text{SIE}}(\phi)$.

In the particular case of the 4th-mode perturbation, an elliptical galaxy would be more discy if $\phi_4 = 0$, and more boxy if $\phi_4 = \pi/4$ (which is the same as in the conventional definition that $\delta R_4(\phi) = a_4 \cos(4\phi)$, where $a_4 > 0$ corresponds to a discy galaxy and $a_4 < 0$ corresponds to a boxy galaxy).

From Eq. (B2) it can be seen that, as the convergence is $\kappa(\theta, \phi) = (R_{\text{SIE}}(\phi) + \sum_m \delta R_m(\phi))(2\theta)^{-1}$, now the new iso- κ contours follow the perturbed ellipse $(R_{\text{SIE}}(\phi) + \sum_m \delta R_m(\phi))$ (at $\kappa = \frac{1}{2}$) and are scaled by θ^{-1} .

The corresponding shape function $F_m(\phi)$ is given by (see Keeton et al. 2003):

$$F_m(\phi) = \frac{1}{1 - m^2} a_m \cos(m(\phi - \phi_m)). \quad (\text{B6})$$

The physical quantity of δR_m in Eq. (B5) is the same as in Hao et al. (2006), where the expression is given by:

$$\delta R_m(\phi) = \alpha_m \cos(m\phi) + \beta_m \sin(m\phi). \quad (\text{B7})$$

In their work, α_m/a and β_m/a (where a is the semi-major axis length of the perfect ellipse) for $m = 3, 4$, and ellipticity $e (\equiv 1 - q)$ of the elliptical isophotes were measured within the Petrosian half-light radii. We use these values in our main lens modelling. Notice that Eq. (B7) can also be re-written as: $\delta R_m(\phi) = \sqrt{\alpha_m^2 + \beta_m^2} \cos(m(\phi - \phi_m))$, where $\phi_m = \frac{1}{m} \tan^{-1}(\beta_m/\alpha_m) \in \frac{1}{m}[0, 2\pi)$. Comparing with Eq. (B5), it can be seen that:

$$\begin{aligned} a_m &= \sqrt{\alpha_m^2 + \beta_m^2} \equiv \sqrt{(\alpha_m/a)^2 + (\beta_m/a)^2} \times a_{\text{SIE}}, \\ \phi_m &= \frac{1}{m} \tan^{-1}(\beta_m/\alpha_m). \end{aligned} \quad (\text{B8})$$

where a_m is re-normalized at $\kappa = \frac{1}{2}$; $a_{\text{SIE}} = \frac{\theta_{\text{Ein}}}{\sqrt{1 - \epsilon}}$ as given in Eq. (B4).

B3 Constant external shear

The lens potential $\psi^{\text{ext}}(\theta, \phi)$ caused by a constant external shear is given by:

$$\psi^{\text{ext}}(\theta, \phi) = -\frac{\gamma_{\text{ext}}}{2} \theta^2 \cos(2(\phi - \phi_{\text{ext}})), \quad (\text{B9})$$

where $\gamma_{\text{ext}} (> 0)$ is the shear amplitude and $\phi_{\text{ext}} \in [0, \pi)$ is the position angle of the shear mass, measured counter-clockwise from the semi-major axis of the isothermal ellipsoid. External shear will not contribute to external convergence, i.e., $\kappa_{\text{ext}} = 0$. In this work, we assume random external shear orientation in each simulated lens system.

REFERENCES

- Amara A., Metcalf R. B., Cox T. J., Ostriker J. P., 2006, *MNRAS*, 367, 1367
- Benson A. J., Frenk C. S., Lacey C. G., Baugh C. M., Cole S., 2002, *MNRAS*, 333, 177
- Biggs A., Browne I., Jackson N., York T., Norbury M., McKean J., Phillips P., 2004, *MNRAS*, 350, 949
- Biggs A. D., Xanthopoulos E., Browne I. W. A., Koopmans L. V. E., Fassnacht C. D., 2000, *MNRAS*, 318, 73
- Blandford R., Narayan R., 1986, *ApJ*, 310, 568
- Bovill M. S., Ricotti M., 2009, *ApJ*, 693, 1859
- Bradač M., Schneider P., Lombardi M., Steinmetz M., Koopmans L. V. E., Navarro J. F., 2004, *A&A*, 423, 797
- Bradač M., Schneider P., Steinmetz M., Lombardi M., King L. J., Porcas R., 2002, *A&A*, 388, 373
- Bullock J. S., Kravtsov A. V., Weinberg D. H., 2000, *ApJ*, 539, 517
- Chen J., Koushiappas S., Zentner A., 2011, *ApJ*, 741, 117
- Chen J., Rozo E., Dalal N., Taylor J., 2007, *ApJ*, 659, 52
- Chiba M., Minezaki T., Kashikawa N., Kataza H., Inoue K. T., 2005, *ApJ*, 627, 53
- Cohn J. D., Kochanek C. S., McLeod B. A., Keeton C. R., 2001, *ApJ*, 554, 1216
- Congdon A. B., Keeton C. R., 2005, *MNRAS*, 364, 1459
- Cooper A. P., Cole S., Frenk C. S., White S. D. M., Helly J., Benson A. J., De Lucia G., Helmi A., Jenkins A., Navarro J. F., Springel V., Wang J., 2010, *MNRAS*, 406, 744
- Dalal N., Kochanek C. S., 2002, *ApJ*, 572, 25
- De Lucia G., Kauffmann G., Springel V., White S. D. M., Lanzoni B., Stoehr F., Tormen G., Yoshida N., 2004, *MNRAS*, 348, 333
- Dobler G., Keeton C. R., 2006, *MNRAS*, 365, 1243
- Einasto J., 1965, *Trudy Inst. Astroz. Alma-Ata*, 51, 87
- Evans N. W., Witt H. J., 2003, *MNRAS*, 345, 1351
- Fadely R., Keeton C. R., 2012, *MNRAS*, 419, 936
- Falco E. E., Impey C. D., Kochanek C. S., Lehár J., McLeod B. A., Rix H.-W., Keeton C. R., Muñoz J. A., Peng C. Y., 1999, *ApJ*, 523, 617
- Falco E. E., Lehar J., Perley R. A., Wambsganss J., Gorenstein M. V., 1996, *AJ*, 112, 897
- Fassnacht C. D., Blandford R. D., Cohen J. G., Matthews K., Pearson T. J., Readhead A. C. S., Womble D. S., Myers S. T., Browne I. W. A., Jackson N. J., Marlow D. R., Wilkinson P. N., Koopmans L., de Bruyn A., Schilizzi R., Bremer M., Miley G., 1999, *AJ*, 117, 658
- Fassnacht C. D., Kocevski D. D., Auger M. W., Lubin L. M., Neureuther J. L., Jeltrema T. E., Mulchaey J. S., McKean J. P., 2008, *ApJ*, 681, 1017
- Fassnacht C. D., Lubin L. M., 2002, *AJ*, 123, 627
- Fassnacht C. D., Womble D. S., Neugebauer G., Browne I. W. A., Readhead A. C. S., Matthews K., Pearson T. J., 1996, *ApJ Letters*, 460, L103
- Font A. S., Benson A. J., Bower R. G., Frenk C. S., Cooper A., De Lucia G., Helly J. C., Helmi A., Li Y.-S., McCarthy I. G., Navarro J. F., Springel V., Starkenburg E., Wang J., White S. D. M., 2011, *MNRAS*, 417, 1260
- Forte J. C., Martinez R. E., Muzzio J., 1982, *AJ*, 87, 1465
- Gao L., Navarro J. F., Frenk C. S., Jenkins A., Springel V., White S. D. M., 2012, *MNRAS*, 425, 2169
- Gao L., White S. D. M., Jenkins A., Stoehr F., Springel V., 2004, *MNRAS*, 355, 819
- Garrett M. A., Muxlow T. W. B., Patnaik A. R., Walsh D., 1994, *MNRAS*, 269, 902
- Grant C. E., Bautz M. W., Chartas G., Garmire G. P., 2004, *ApJ*, 610, 686
- Guo Q., White S., Boylan-Kolchin M., De Lucia G., Kauffmann G., Lemson G., Li C., Springel V., Weinmann S., 2011, *MNRAS*, 413, 101
- Hao C. N., Mao S., Deng Z. G., Xia X. Y., Wu H., 2006, *MNRAS*, 370, 1339
- Harris W. E., 1991, *Annual Review of Astronomy and Astrophysics*, 29, 543
- Harris W. E., 1993, in G. H. Smith & J. P. Brodie ed., *The Globular Cluster-Galaxy Connection Vol. 48 of Astronomical Society of the Pacific Conference Series, Photometric Properties of Globular Cluster Systems in Large Galaxies*. p. 472
- Hezaveh Y., Dalal N., Holder G., Kuhlen M., Marrone D., Murray N., Vieira J., 2013, *ApJ*, 767, 9
- Impey C. D., Foltz C. B., Petry C. E., Browne I. W. A., Patnaik A. R., 1996, *ApJ Letters*, 462, L53
- Jackson N., 2011, *ApJ Letters*, 739, L28
- Jackson N., Nair S., Browne I. W. A., Wilkinson P. N., Muxlow T. W. B., de Bruyn A. G., Koopmans L., Bremer M., Snellen I., Miley G. K., Schilizzi R. T., Myers S., Fassnacht C. D., Womble D. S., Readhead A. C. S., Blandford R. D., Pearson T. J., 1998, *MNRAS*, 296, 483
- Jackson N., Xanthopoulos E., Browne I. W. A., 2000, *MNRAS*, 311, 389
- Kassiola A., Kovner I., 1993, *ApJ*, 417, 450
- Katz C. A., Moore C. B., Hewitt J. N., 1997, *ApJ*, 475, 512
- Keeton C. R., 2003, *ApJ*, 584, 664
- Keeton C. R., Gaudi B. S., Petters A., 2003, *ApJ*, 598, 138
- Keeton C. R., Gaudi B. S., Petters A., 2005, *ApJ*, 635, 35
- Keeton C. R., Kochanek C., Falco E., 1998, *ApJ*, 509, 561
- Keeton C. R., Kochanek C., Seljak U., 1997, *ApJ*, 482, 604
- Keeton C. R., Kochanek C. S., 1998, *ApJ*, 495, 157
- Klypin A., Kravtsov A. V., Valenzuela O., Prada F., 1999, *ApJ*, 522, 82
- Kochanek C. S., 1991, *ApJ*, 373, 354
- Kochanek C. S., Dalal N., 2004, *ApJ*, 610, 69
- Kochanek C. S., Falco E. E., Impey C. D., Lehár J., McLeod B. A., Rix H.-W., Keeton C. R., Muñoz J. A., Peng C. Y., 2000, *ApJ*, 543, 131
- Komatsu E., Dunkley J., Nolte M. R., Bennett C. L., Gold B., Hinshaw G., Jarosik N., Larson D., Limon M., Page L., Spergel D. N., Halpern M., Hill R. S., Kogut A., Meyer S. S., Tucker G. S., Weiland J. L., Wollack E., Wright E. L., 2009, *ApJ Suppl.*, 180, 330
- Koopmans L. V. E., Biggs A., Blandford R. D., Browne I. W. A., Jackson N. J., Mao S., Wilkinson P. N., de Bruyn A. G., Wambsganss J., 2003, *ApJ*, 595, 712
- Koopmans L. V. E., Fassnacht C. D., 1999, *ApJ*, 527, 513
- Koopmans L. V. E., Treu T., 2002, *ApJ Letters*, 568, L5
- Koopmans L. V. E., Bolton A. S., Burles S., Moustakas L. A., 2006, *ApJ*, 649, 599
- Koposov S., Belokurov V., Evans N. W., Hewett P. C., Irwin M. J., Gilmore G., Zucker D. B., Rix H.-W., Fellhauer M., Bell E. F., Glushkova E. V., 2008, *ApJ*, 686, 279
- Koposov S. E., Yoo J., Rix H.-W., Weinberg D. H., Macciò A. V., Escudé J. M., 2009, *ApJ*, 696, 2179
- Kormann R., Schneider P., Bartelmann M., 1994, *A&A*, 284, 285

- Kravtsov A., Gnedin O., Klypin A., 2004, *ApJ*, 609, 482
- Lawrence C. R., Elston R., Januzzi B. T., Turner E. L., 1995, *AJ*, 110, 2570
- Ludlow A. D., Navarro J. F., Boyle-Kolchin M., Bett P. E., Angulo R. E., Li M., White S. D. M., Frenk C., Springel V., 2013, *MNRAS*, 432, 1103
- Macciò A. V., Miranda M., 2006, *MNRAS*, 368, 599
- Macciò A. V., Moore B., Stadel J., Diemand J., 2006, *MNRAS*, 366, 1529
- McLeod C. L., Jones R., Agol E., Kochanek C. S., 2013, *ApJ*, 773, 35
- Maller A., Simard L., Guhathakurta P., Hjorth J., Jaunsen A., Flores R., Primack J., 2000, *ApJ*, 533, 194
- Mao S., 1992, *ApJ*, 389, 63
- Mao S., Jing Y., Ostriker J. P., Weller J., 2004, *ApJ Letters*, 604, L5
- Mao S., Schneider P., 1998, *MNRAS*, 295, 587
- Marlow D. R., Myers S. T., Rusin D., Jackson N., Browne I. W. A., Wilkinson P. N., Muxlow T., Fassnacht C. D., Lubin L., Kundić T., Blandford R. D., Pearson T. J., Readhead A. C. S., Koopmans L., de Bruyn A. G., 1999, *AJ*, 118, 654
- McKean J. P., Koopmans L. V. E., Flack C. E., Fassnacht C. D., Thompson D., Matthews K., Blandford R. D., Readhead A. C. S., Soifer B. T., 2007, *MNRAS*, 378, 109
- Metcalf R. B., 2005a, *ApJ*, 622, 72
- Metcalf R. B., 2005b, *ApJ*, 629, 673
- Metcalf R. B., Amara A., 2012, *MNRAS*, 419, 3414
- Metcalf R. B., Madau P., 2001, *ApJ*, 563, 9
- Metcalf R. B., Zhao H., 2002, *ApJ Letters*, 567, L5
- Minezaki T., Chiba M., Kashikawa N., Inoue K. T., Kataza H., 2009, *ApJ*, 697, 610
- Miranda M., Macciò A. V., 2007, *MNRAS*, 382, 1225
- Möller O., Hewett P., Blain A. W., 2003, *MNRAS*, 345, 1
- Momcheva I., Williams K., Keeton C., Zabludoff A., 2006, *ApJ*, 641, 169
- Moore B., Ghigna S., Governato F., Lake G., Quinn T., Stadel J., Tozzi P., 1999, *ApJ Letters*, 524, L19
- Nierenberg A. M., Treu T., Wright S. A., Fassnacht C. D., Auger M. W., 2014, *MNRAS*, 442, 2434
- Patnaik A. R., Browne I. W. A., Walsh D., Chaffee F. H., Foltz C. B., 1992, *MNRAS*, 259, 1P
- Patnaik A. R., Kembal A. J., Porcas R. W., Garrett M. A., 1999, *MNRAS*, 307, L1
- Pettters A. O., Levine H., Wambsganss J., 2001, Singularity theory and gravitational lensing
- Phillips P. M., Norbury M. A., Koopmans L. V. E., Browne I. W. A., Jackson N. J., Wilkinson P. N., Biggs A. D., Blandford R. D., de Bruyn A. G., Fassnacht C. D., Hellig P., Mao S., Marlow D. R., Myers S. T., Pearson T. J., Readhead A. C. S., Rusin D., Xanthopoulos E., 2000, *MNRAS*, 319, L7
- Planck Collaboration Ade P. A. R., Aghanim N., Armitage-Caplan C., Arnaud M., Ashdown M., Atrio-Barandela F., Aumont J., Baccigalupi C., Banday A. J., et al. 2014, *A&A*, 571, A16
- Ros E., Guirado J., Marcaide J., Pérez-Torres M., Falco E., Muñoz J., Alberdi A., Lara L., 2000, *A&A*, 362, 845
- Rozo E., Zentner A. R., Bertone G., Chen J., 2006, *ApJ*, 639, 573
- Rusin D., Kochanek C. S., Falco E. E., Keeton C. R., McLeod B. A., Impey C. D., Lehár J., Muñoz J. A., Peng C. Y., Rix H.-W., 2003, *ApJ*, 587, 143
- Rusin D., Kochanek C. S., Norbury M., Falco E. E., Impey C. D., Lehár J., McLeod B. A., Rix H.-W., Keeton C. R., Muñoz J. A., Peng C. Y., 2001, *ApJ*, 557, 594
- Schechter P. L., Wambsganss J., 2002, *ApJ*, 580, 685
- Schneider P., Ehlers J., Falco E. E., 1992, Gravitational Lenses. XIV, p. 560, Springer-Verlag Berlin Heidelberg New York
- Schneider P., Weiss A., 1992, *A&A*, 260, 1
- Shin E. M., Evans N. W., 2008, *MNRAS*, 385, 2107
- Sluse D., Chantry V., Magain P., Courbin F., Meylan G., 2012, *A&A*, 538, A99
- Sluse D., Kishimoto M., Anguita T., Wucknitz O., Wambsganss J., 2013, *A&A*, 553, A53
- Spergel D. N., Verde L., Peiris H. V., Komatsu E., Nolte M. R., Bennett C. L., Halpern M., Hinshaw G., Jarosik N., Kogut A., Limon M., Meyer S. S., Page L., Tucker G. S., Weiland J. L., Wollack E., Wright E. L., 2003, *ApJ Suppl.*, 148, 175
- Springel V., Wang J., Vogelsberger M., Ludlow A., Jenkins A., Helmi A., Navarro J. F., Frenk C. S., White S. D. M., 2008, *MNRAS*, 391, 1685
- Surpi G., Blandford R. D., 2003, *ApJ*, 584, 100
- Suyu S. H., Hensel S. W., McKean J. P., Fassnacht C. D., Treu T., Halkola A., Norbury M., Jackson N., Schneider P., Thompson D., Auger M. W., Koopmans L. V. E., Matthews K., 2012, *ApJ*, 750, 10
- Sykes C. M., Browne I. W. A., Jackson N. J., Marlow D. R., Nair S., Wilkinson P. N., Blandford R. D., Cohen J., Fassnacht C. D., Hogg D., Pearson T. J., Readhead A. C. S., Womble D. S., Myers S. T., de Bruyn A. G., Bremer M., Miley G. K., Schilizzi R. T., 1998, *MNRAS*, 301, 310
- Thomas D., Maraston C., Bender R., Mendes de Oliveira C., 2005, *ApJ*, 621, 673
- Tollerud E. J., Bullock J. S., Strigari L. E., Willman B., 2008, *ApJ*, 688, 277
- van de Ven G., van Dokkum P. G., Franx M., 2003, *MNRAS*, 344, 924
- Vegetti S., Koopmans L. V. E., 2009, *MNRAS*, 400, 1583
- Vegetti S., Koopmans L. V. E., Auger M. W., Treu T., Bolton A. S., 2014, *MNRAS*, 442, 2017
- Vegetti S., Lagattuta D. J., McKean J. P., Auger M. W., Fassnacht C., Koopmans L., 2012, *Nature*, 481, 341
- Vera-Ciro C. A., Helmi A., Starkeburg E., Breddels M. A., 2013, *MNRAS*, 428, 1696
- Wang J., Frenk C. S., Navarro J. F., Gao L., Sawala T., 2012, *MNRAS*, 424, 2715
- West M. J., 1993, *MNRAS*, 265, 755
- Wong K. C., Keeton C. R., Williams K. A., Momcheva I. G., Zabludoff A. I., 2011, *ApJ*, 726, 84
- Xu D. D., Mao S., Cooper A. P., Gao L., Frenk C. S., Angulo R. E., Helly J., 2012, *MNRAS*, 421, 2553
- Xu D. D., Mao S., Cooper A. P., Wang J., Gao L., Frenk C. S., Springel V., 2010, *MNRAS*, 408, 1721
- Xu D. D., Mao S., Wang J., Springel V., Gao L., White S. D. M., Frenk C. S., Jenkins A., Li G., Navarro J. F., 2009, *MNRAS*, 398, 1235
- Yoo J., Kochanek C. S., Falco E. E., McLeod B. A., 2006, *ApJ*, 642, 22
- Zakharov A. F., 1995, *A&A*, 293, 1
- Zentner A. R., Berlind A. A., Bullock J. S., Kravtsov A. V., Wechsler R. H., 2005, *ApJ*, 624, 505